

Copyright © 1989, by the author(s).
All rights reserved.

Permission to make digital or hard copies of all or part of this work for personal or classroom use is granted without fee provided that copies are not made or distributed for profit or commercial advantage and that copies bear this notice and the full citation on the first page. To copy otherwise, to republish, to post on servers or to redistribute to lists, requires prior specific permission.

**DETERMINING THE AXIS OF A SURFACE
OF REVOLUTION USING TACTILE SENSING**

by

Matthew D. Berkemeier and Ronald S. Fearing

Memorandum No. UCB/ERL M89/117

3 October 1989

COVER PAGE

**DETERMINING THE AXIS OF A SURFACE
OF REVOLUTION USING TACTILE SENSING**

by

Matthew D. Berkemeier and Ronald S. Fearing

Memorandum No. UCB/ERL M89/117

3 October 1989

ELECTRONICS RESEARCH LABORATORY

College of Engineering
University of California, Berkeley
94720

TITLE PAGE

**DETERMINING THE AXIS OF A SURFACE
OF REVOLUTION USING TACTILE SENSING**

by

Matthew D. Berkemeier and Ronald S. Fearing

Memorandum No. UCB/ERL M89/117

3 October 1989

ELECTRONICS RESEARCH LABORATORY

College of Engineering
University of California, Berkeley
94720

Determining the Axis of a Surface of Revolution Using Tactile Sensing

Matthew D. Berkemeier

Ronald S. Fearing

Department of Electrical Engineering and Computer Science
Electronics Research Laboratory
University of California, Berkeley, CA 94720

ABSTRACT

Dextrous robot hands need to be able to determine the position and orientation of objects to reliably grasp and manipulate them. The use of fingertip tactile sensors to provide this feedback is an attractive but underdeveloped approach; moreover, algorithms for vision systems are not directly applicable since a rich set of sensory data from the object is typically assumed. Sparse tactile sensing can be used to determine the location and orientation of an unknown object, given a well-chosen class constraint but not a specific model. This paper considers a simple example of exploiting class constraints: finding the axis of an unknown surface of revolution. Three tactile curvature measurements on a surface of revolution with sweeping rule in C^2 are shown to be sufficient for determining the axis except for certain singular configurations. Experimental results and position and orientation error bounds are presented using a capacitive tactile sensor.

Determining the Axis of a Surface of Revolution Using Tactile Sensing

Matthew D. Berkemeier

Ronald S. Fearing

Department of Electrical Engineering and Computer Science
Electronics Research Laboratory
University of California, Berkeley, CA 94720

1. Introduction

Dextrous robot hands need to be able to determine the position and orientation of objects to reliably grasp and manipulate them. Fingertip-mounted tactile sensors are an attractive means for providing this feedback since, in addition to reliably supplying the contact location and surface normal (in our case, also the curvature directions and magnitudes), the force applied can be determined at each contact, and this is important for grasping.

It is easiest, initially, to seek a method in which the position and orientation are determined from a single grasp. This avoids the problem of the object changing position while the fingers move to explore new contacts. On the other hand, this means that the position and orientation must be computed from relatively sparse data, and therefore, algorithms for vision systems which assume a rich set of sensory data are not directly applicable.

We will ignore for now the problems of finding the object in the workspace and achieving a stable grasp and concentrate instead on the problem of determining the position and orientation of a fixed object from the sensory information at a few contacts.

There have been two main methods of determining the shape and properties of an object from sensory data. We distinguish here between model matching and shape description without specific models.

Model matching can localize and identify objects by comparing relations between sensed features and features on particular object models. A consistent combination of features in the world and in the model determines the object and its position and orientation but not necessarily uniquely. For example, Gaston and Lozano-Perez [1983] and Faugeras and Hebert [1986] assume known objects and determine object shape, location, and orientation by matching features in the world to specific object models, keeping all consistent matches. Ellis [1987] has extended this work by developing a planning system to choose tactile sensor paths, using prior sensed data, that will prune an interpretation

tree more efficiently.

Shape description uses measurements and geometric constraints to derive a representation of the object and does not require prior object models. It has been the focus of much research lately since it enables a sensory system to deal with many more objects than is practical for model matching. Typically, the objects to be dealt with are assumed to be of a certain class. There is a tradeoff, however, in using an object class versus specific object models: In general, the less that is assumed about the object, the less that can be said about the object from the same amount of sensory data. It is important, then, to choose an object class that adequately covers the objects to be dealt with, yet is not so general as to make it difficult to say anything about the object. In tactile sensing this is especially important since we wish to determine as much as possible from only the few contacts made during a single grasp. Brady et al [1984] use range finder data to describe surfaces in terms of bounding contours, surface intersections, lines of curvature, and asymptotes. Also, they demonstrate finding the axis of a surface of revolution using lines of curvature, which is relevant to this work. Allen [1986] describes objects in terms of surface patches (Coons' patches) and builds up a representation of the object with a tactile sensor, in combination with vision, by exploration over the whole object. Cole and Yap [1987] assume polygonal objects and describe algorithms which determine the shape using "probes" that determine only the contact location. Rao and Nevatia [1988] use a class of linear straight homogeneous generalized cylinders and, using both synthetic data and real data from a feature-based stereo system, solve for the representations of cones and cylinders of various cross sections. Notably, they allow noisy edge detector data (e.g., broken and false edges). Allen and Roberts [1989] assume that objects can be adequately represented by superquadrics and, using the points of contact that a Utah/MIT hand makes with the object, calculate the superquadric and rotation/position parameters. Printz [1987] presupposes cones or cylinders of circular or elliptical cross section and finds the generating axis by analyzing the Extended Gaussian Image of the object. Grimson [1987] assumes all objects to be encountered are in a model database but allows certain parameters to be "free," e.g., the length of the object or the angle of a joint.

This paper is another example of the shape description method. The particular object class that we have chosen is the surface of revolution. While not a very general class of objects, they are common in man-made environments. Unlike most of the work presented above, we assume sparse sensing. Nevertheless, our method for determining the axis is applicable to any surface of revolution with sweeping rule in C^2 . This is due to the special properties of this particular class of objects.

In section 2 we describe two possible methods for determining the axis. The first uses the contact location, surface normal, and principal curvature magnitudes at three contacts, while the second uses the contact location, surface normal, and principal curvature directions at three contacts. All possible singular configurations are then derived in section 3 for the latter method. Section 4 is a simple error analysis for both of the methods based on the errors of the tactile sensor of [Fearing and Binford, 1988]. Section 5 contains experimental results for our method. Section 6 contains our conclusions, and section 7 is an appendix with some comments on the curvature from strain problem.

This paper extends previous work [Fearing, 1990] which showed how the axis and orientation of unknown simple cones (linear straight homogeneous generalized cylinders) could be determined from a minimum of three independent curvature measurements.

2. Surface of Revolution Geometry

In this section we derive the basic equations for the curvature magnitudes and curvature directions for a surface of revolution. Two methods for determining the axis of a surface of revolution are also described.

2.1. Notation

We will use the following notation:

\underline{p} , a vector to the point of contact on the surface of revolution.

\hat{k}_1, \hat{k}_2 , unit vectors of the two principal directions of curvature.

κ_1, κ_2 , magnitudes of the curvature along the two above principal directions. κ_1 is along \hat{k}_1 , and κ_2 is along \hat{k}_2 .

\hat{n} , the unit surface normal at the contact point.

Our tactile sensor is capable of determining each of these parameters at a point on an object [Fearing and Binford, 1988].

2.2. Basic Equations

For simplicity, we choose a coordinate system such that the z -axis coincides with the axis of the surface of revolution under consideration.

The surface of revolution can be described by the vector equation [Ponce, 1987]

$$\underline{x}(\theta, z) = \begin{bmatrix} r(z)\cos\theta \\ r(z)\sin\theta \\ z \end{bmatrix}, \quad (1)$$

where $r(\cdot)$ is a function describing the curve which is rotated about the z -axis to generate

the surface of revolution.

We first calculate the unit surface normal directed out of the surface of revolution.

$$\hat{n} = \frac{\underline{x}_\theta \times \underline{x}_z}{|\underline{x}_\theta \times \underline{x}_z|} = \frac{1}{\sqrt{r'^2(z)+1}} \begin{bmatrix} \cos\theta \\ \sin\theta \\ -r'(z) \end{bmatrix}. \quad (2)$$

Next, we calculate the first (E, F, G) and second (L, M, N) fundamental coefficients [Lipschutz, 1969]

$$E = \underline{x}_\theta \cdot \underline{x}_\theta = r^2(z) \quad (3)$$

$$F = \underline{x}_\theta \cdot \underline{x}_z = 0 \quad (4)$$

$$G = \underline{x}_z \cdot \underline{x}_z = r'^2(z) + 1 \quad (5)$$

$$L = \underline{x}_{\theta\theta} \cdot (-\hat{n}) = \frac{r(z)}{\sqrt{r'^2(z)+1}} \quad (6)$$

$$M = \underline{x}_{\theta z} \cdot (-\hat{n}) = 0 \quad (7)$$

$$N = \underline{x}_{zz} \cdot (-\hat{n}) = \frac{-r''(z)}{\sqrt{r'^2(z)+1}}. \quad (8)$$

where we have used the notation

$$\underline{x}_\theta = \frac{\partial}{\partial \theta} \underline{x}(\theta, z) \quad (9)$$

(similarly for \underline{x}_z),

$$\underline{x}_{\theta\theta} = \frac{\partial^2}{\partial \theta^2} \underline{x}(\theta, z) \quad (10)$$

(similarly for \underline{x}_{zz} and $\underline{x}_{\theta z}$), and

$$r'(z) = \frac{d}{dz} r(z). \quad (11)$$

Notice we have taken the dot product with $(-\hat{n})$ instead of \hat{n} in equations (6) - (8). Thus, a positive principal curvature will correspond to a convex curve on the surface of revolution. \hat{k}_1 and \hat{k}_2 , the two principal directions, are of the form

$$\hat{k}_i = \underline{x}_\theta d\theta_i + \underline{x}_z dz_i, \quad i=1, 2, \quad (12)$$

where $d\theta_i$ and dz_i are the solutions to the equation [Lipschutz, 1969]

$$(EM - LF) d\theta_i^2 + (EN - LG) d\theta_i dz_i + (FN - MG) dz_i^2 = 0, \quad i=1, 2. \quad (13)$$

Since F and M are zero, it follows that the two solutions are

$$dz_1 = c_1, \quad d\theta_1 = 0, \quad (14)$$

and

$$dz_2 = 0, \quad d\theta_2 = c_2, \quad (15)$$

where c_1 and c_2 are arbitrary constants. Substitution into (12) and normalizing gives

$$\hat{k}_z = \frac{1}{\sqrt{r'^2(z)+1}} \begin{bmatrix} r'(z)\cos\theta \\ r'(z)\sin\theta \\ 1 \end{bmatrix}, \quad (16)$$

where we have chosen to use \hat{k}_z instead of \hat{k}_1 since the direction is simply \underline{x}_z . Similarly,

$$\hat{k}_\theta = \begin{bmatrix} -\sin\theta \\ \cos\theta \\ 0 \end{bmatrix}, \quad (17)$$

where we have again chosen a more descriptive subscript for the principal direction. To solve for the magnitudes of the principal curvatures we will use the equation [Lipschutz, 1969]

$$\kappa_i = \frac{Ld\theta_i^2 + 2Md\theta_i dz_i + Ndz_i^2}{Ed\theta_i^2 + 2Fd\theta_i dz_i + Gdz_i^2}, \quad i = 1, 2. \quad (18)$$

Again using the fact that $F = M = 0$

$$\kappa_z = \frac{N}{G} = \frac{-r''(z)}{[r'^2(z)+1]^{1.5}}, \quad (19)$$

$$\kappa_\theta = \frac{L}{E} = \frac{1}{r(z)\sqrt{r'^2(z)+1}}, \quad (20)$$

where κ_z is the curvature along \hat{k}_z and κ_θ is the curvature along \hat{k}_θ .

The lines of curvature which have \hat{k}_θ as tangent vectors are parallels, and meridians have \hat{k}_z tangent vectors. Figure 1 illustrates these curves.

2.3. Finding a Point on and a Plane Through the Axis

The information calculated from each contact on a surface of revolution is

$$\{ \kappa_\theta, \kappa_z, \hat{k}_\theta, \hat{k}_z, \hat{n}, \underline{p} \}$$

[Fearing and Binford, 1988]. Notice that this set is defined by eight independent parameters. Three are needed to define \underline{p} , two are needed to define \hat{n} (since it has unit length), one is needed for \hat{k}_z and \hat{k}_θ once \hat{n} is defined (since they have unit length and are perpendicular to one another and to \hat{n}), and one is needed for each of the curvature magnitudes.

Figure 1 illustrates κ_θ , \hat{k}_θ , \hat{k}_z , and \hat{n} . Notice that $\frac{1}{\kappa_\theta}$ is the distance from the surface to

the axis measured normal to the surface, not normal to the axis, as one might first assume.

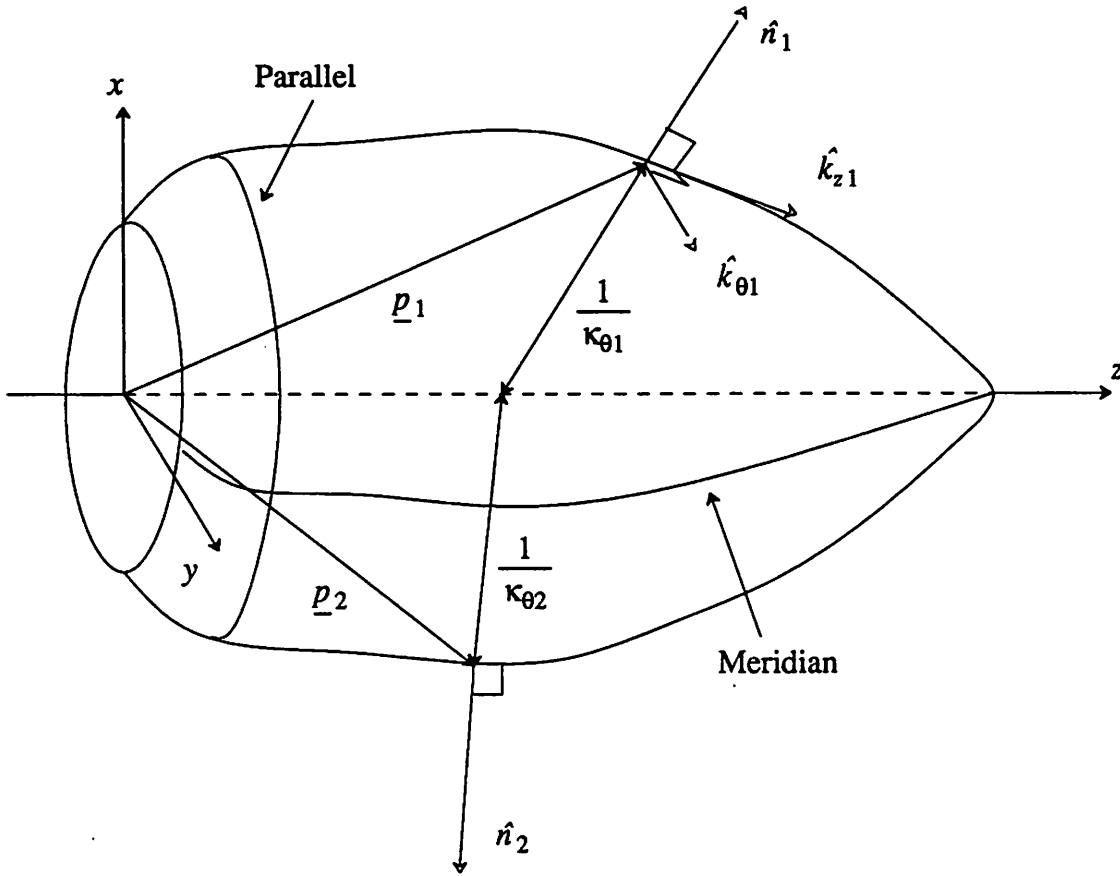


Figure 1. A Surface of Revolution

Given several contacts on an unknown surface of revolution, we want to use contact information at these points to determine the axis of the surface of revolution. We can find a point on the axis by

$$\begin{aligned} \underline{p} - \frac{1}{\kappa_{\theta}} \hat{n} &= \begin{bmatrix} r(z)\cos\theta \\ r(z)\sin\theta \\ z \end{bmatrix} - r(z)\sqrt{r'^2(z)+1} \frac{1}{\sqrt{r'^2(z)+1}} \begin{bmatrix} \cos\theta \\ \sin\theta \\ -r'(z) \end{bmatrix} \\ &= \begin{bmatrix} 0 \\ 0 \\ r(z)r'(z)+z \end{bmatrix}. \end{aligned} \quad (21)$$

We can find a plane which includes the axis by

$$\underline{p} + s\hat{n} + t\hat{k}_z = \frac{1}{\sqrt{r'^2(z)+1}} \begin{bmatrix} \left[r(z)\sqrt{r'^2(z)+1} + s + tr'(z) \right] \cos\theta \\ \left[r(z)\sqrt{r'^2(z)+1} + s + tr'(z) \right] \sin\theta \\ z\sqrt{r'^2(z)+1} - sr'(z) + t \end{bmatrix}, \quad (22)$$

where s and t are free variables which parameterize the plane. A more useful representation is in the form of the plane equation

$$ax + by + cz = d, \quad (23)$$

where (a, b, c) are the components of a unit vector perpendicular to the plane and d is the perpendicular distance to the plane from the origin. First, notice that \hat{k}_θ is a unit vector perpendicular to the plane, so we have $a, b,$ and c . Now, notice that the plane (22) passes through the origin since by equating (22) to the zero vector we have a consistent set of two equations and two unknowns (This can also be seen by substituting (x, y, z) from equation (1) into the plane equation with (a, b, c) determined by \hat{k}_θ). Therefore, we can represent the plane as

$$-\sin\theta x + \cos\theta y = 0. \quad (24)$$

Clearly, any point on the axis of the surface of revolution (z -axis) satisfies this equation. (21) and (24) can be used in principle to determine the axis of a surface of revolution from several contacts. Notice that the equation for the point on the axis involves the curvature magnitudes but not the directions, while the equation for the plane through the axis involves the curvature directions but not the magnitudes.

2.4. Determining the Axis

We consider two methods for determining the axis. The first uses the curvature magnitudes but not the directions, while the second uses the curvature directions but not the magnitudes. An intuitive explanation of the methods is the following: From equation (21), κ_θ , along with \hat{n} and \underline{p} , determine a point on the axis. Therefore, the axis can be determined simply by constructing a line through two axis points determined from a pair of contacts. From equation (22), \hat{k}_z , along with \hat{n} and \underline{p} , determine a plane which includes the axis. The intersection of two of these planes is a line which is the axis of the surface of revolution. Note that at least three contacts are actually needed to determine the axis using either of these two methods. The reason is that *a priori* we do not know the correct labeling of the curvature data (i.e., we have no way of distinguishing κ_θ from κ_z and \hat{k}_θ from \hat{k}_z). In order to label or *match* the two \hat{k} directions and two magnitudes, we need a third contact so that we can find a common line generated by all pairs of contacts.

Note also that it is theoretically possible to determine the axis of a surface of revolution from only two contacts if we consider both the curvature magnitudes and the curvature directions at each contact point. In this section we look at information from two contacts, assuming that the principal directions and magnitudes are correctly matched. In section 3 we solve for conditions (singular configurations) on the contact placement which will prevent the matching from being done for the curvature direction method.

2.4.1. Determining Axis Using Curvature Magnitudes

When considering only the magnitudes of curvature, we can specify the axis by

$$(1-s) \left[\underline{p}_1 - \frac{1}{\kappa_{\theta 1}} \hat{n}_1 \right] + s \left[\underline{p}_2 - \frac{1}{\kappa_{\theta 2}} \hat{n}_2 \right], \quad (25)$$

where s parameterizes the axis and subscripts 1 and 2 denote parameters associated with the first and second contacts, respectively. We can determine the axis using curvature magnitudes if and only if

$$\left\| \left[\underline{p}_2 - \frac{1}{\kappa_{\theta 2}} \hat{n}_2 \right] - \left[\underline{p}_1 - \frac{1}{\kappa_{\theta 1}} \hat{n}_1 \right] \right\| \neq 0. \quad (26)$$

Thus, a necessary condition is that the two contact points are not in the same cross-section plane, i.e.,

$$z_1 \neq z_2. \quad (27)$$

This is not a sufficient condition, however. From (21) we see that a sufficient condition is

$$\left[r(z_2)r'(z_2) + z_2 \right] - \left[r(z_1)r'(z_1) + z_1 \right] \neq 0, \quad (28)$$

which means that the surface normals must not intersect on the axis. An example of where (28) is violated but (27) is not can be seen in Figure 1.

2.4.2. Determining Axis Using Curvature Directions

Now consider the problem of determining the surface of revolution axis using only the curvature directions. The axis is determined by the intersection of planes defined by \hat{k}_z , \hat{n} , and \underline{p} . From (24) the two planes can be written as,

$$-\sin\theta_1 x + \cos\theta_1 y = 0 \quad (29)$$

$$-\sin\theta_2 x + \cos\theta_2 y = 0. \quad (30)$$

We can represent the intersection line as a point plus a direction multiplied by a free parameter, s . Since both planes pass through the origin, $\underline{0}$ will be our point. The direction

of intersection is obtained from

$$\begin{bmatrix} -\sin\theta_1 \\ \cos\theta_1 \\ 0 \end{bmatrix} \times \begin{bmatrix} -\sin\theta_2 \\ \cos\theta_2 \\ 0 \end{bmatrix} = \begin{bmatrix} 0 \\ 0 \\ \sin(\theta_2 - \theta_1) \end{bmatrix}. \quad (31)$$

Therefore, the line of intersection can be simply written as

$$s \begin{bmatrix} 0 \\ 0 \\ \sin(\theta_2 - \theta_1) \end{bmatrix}. \quad (32)$$

The necessary and sufficient condition for being able to determine the axis is thus

$$\sin(\theta_2 - \theta_1) \neq 0, \quad (33)$$

or

$$|\theta_2 - \theta_1| \neq n 180^\circ, \quad n = 0, 1, 2, \dots \quad (34)$$

3. The Matching Problem

Recall that we have no way initially of distinguishing \hat{k}_θ from \hat{k}_z . We must therefore consecutively assume particular labels for our curvature directions and then check for global consistency (with the surface of revolution constraints) at all three contacts for each possibility (This was why we needed three contacts instead of just two). We show that, similar to the *general position* assumption made in edge matching problems in vision work [Nevatia, 1982], assuming the contacts are not in particular singular configurations, we will be able to match the curvature directions (i.e., label the principal directions as \hat{k}_θ or \hat{k}_z). Like the edge matching problem, local information alone cannot provide the solution, but when independent local information is combined and considered globally, the solution emerges. Assuming perfect data, we now derive conditions for singular configurations which prevent us from labeling the curvature directions uniquely. Singular configurations imply that the axis cannot be determined uniquely, or in some cases, that it cannot be determined at all.

From the previous section, we know that matched curvature directions enable us to determine the axis of an arbitrary surface of revolution except for certain singular configurations (i.e., equation (34)). In this section we must consider the intersection of three planes, each plane being determined from a contact. Since each contact defines two such planes (the desired plane, perpendicular to \hat{k}_θ , and the undesired plane, perpendicular to \hat{k}_z), there will be a total of $2^3 = 8$ different possible intersections. We show that, assuming the contacts are not in particular singular configurations and assuming perfect

data, one of the intersections is a line (which is the axis) while the other intersections are not lines.

3.1. Intersections of Three Planes

Three arbitrary planes in space will intersect in one of eight ways (See Figure 2, noting that in cases 1 through 7 the planes are viewed edge on).

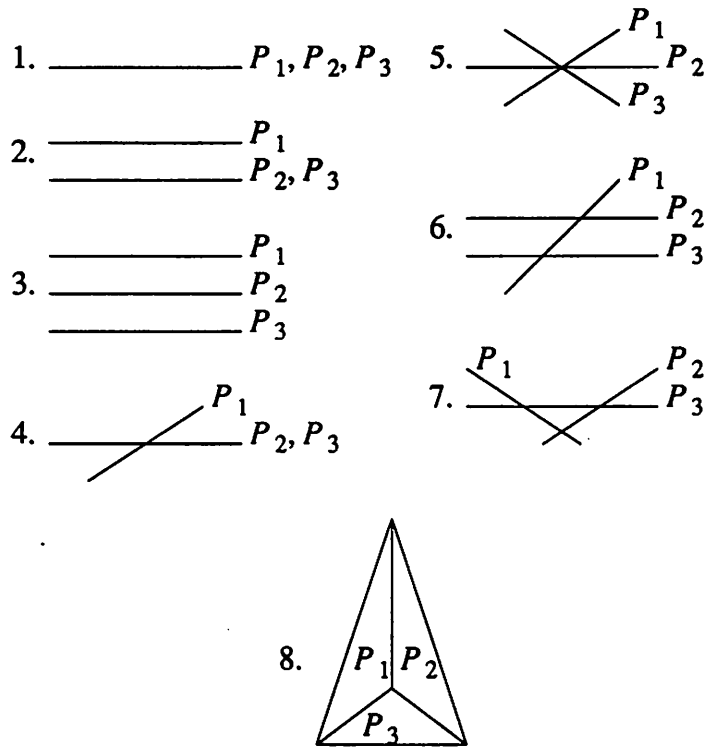


Figure 2. Possible Intersections of Three Planes

The equations for three planes can be written as

$$\begin{bmatrix} a_1 & b_1 & c_1 \\ a_2 & b_2 & c_2 \\ a_3 & b_3 & c_3 \end{bmatrix} \begin{bmatrix} x \\ y \\ z \end{bmatrix} = \begin{bmatrix} d_1 \\ d_2 \\ d_3 \end{bmatrix}, \quad (35)$$

or

$$A\underline{x} = \underline{d}, \quad (36)$$

where (a_i, b_i, c_i) are the components of a unit vector perpendicular to plane i , and d_i is the perpendicular distance to plane i from the origin. The rank of A and $[A \ \underline{d}]$ are listed for each of the possible intersections in Table 1.

Case	Rank A	Rank [A \underline{d}]
1	1	1
2	1	2
3	1	2
4	2	2
5	2	2
6	2	3
7	2	3
8	3	3

Table 1. Conditions on Intersections of Three Planes

Our procedure of analysis will be the following: First we look at the possibilities for the intersections of three correctly matched planes (i.e., planes defined by \hat{n} and \hat{k}_z at each contact). Then we derive conditions under which a combination of incorrectly and correctly matched planes could also yield these same types of intersections. These, in addition to intersections of correctly matched planes which do not intersect in lines, will be our singular configurations since in these cases there will be no way to determine the axis of the surface of revolution. Figure 3 is a simple example of a singular configuration. Incorrectly matched planes P_1 , P_2 , and P_3 (which are viewed edge on) intersect in a line perpendicular to the page. Notice also that the correctly matched planes are coincident (they are in the plane of the page), and thus the actual axis could not be determined by this configuration. Any set of data where one labeling produces three coincident planes will require additional tactile data.

3.2. Intersection of Correctly Matched Planes

Consider the following three planes (see equation (24)):

$$P_1: -\sin\theta_1 x + \cos\theta_1 y = 0 \quad (37)$$

$$P_2: -\sin\theta_2 x + \cos\theta_2 y = 0 \quad (38)$$

$$P_3: -\sin\theta_3 x + \cos\theta_3 y = 0. \quad (39)$$

Therefore, we have

$$A = \begin{bmatrix} -\sin\theta_1 & \cos\theta_1 & 0 \\ -\sin\theta_2 & \cos\theta_2 & 0 \\ -\sin\theta_3 & \cos\theta_3 & 0 \end{bmatrix}, \quad \underline{d} = \begin{bmatrix} 0 \\ 0 \\ 0 \end{bmatrix}. \quad (40)$$

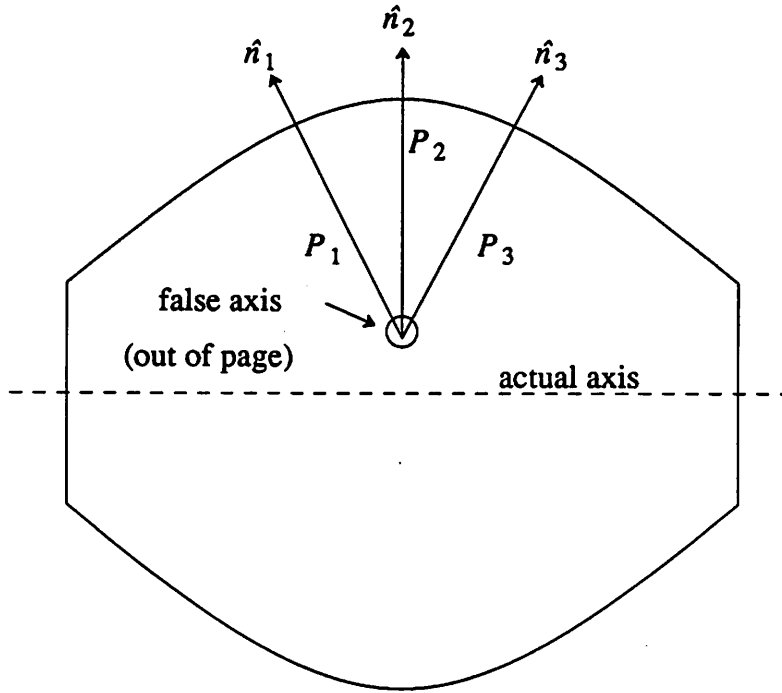


Figure 3. A Singular Configuration

By using Gaussian elimination we can determine the rank of A and $[A \ \underline{d}]$.

$$[A \ \underline{d}] \rightarrow \begin{bmatrix} -\sin\theta_1 & \cos\theta_1 & 0 & 0 \\ 0 & \sin(\theta_1 - \theta_2) & 0 & 0 \\ 0 & \sin(\theta_1 - \theta_3) & 0 & 0 \end{bmatrix}. \quad (41)$$

Therefore, $\text{rank } A = \text{rank } [A \ \underline{d}]$, and we have the possibilities listed in Table 2. Notice that we have made the assumption that $-\sin\theta_1 \neq 0$. This assumption is always valid since by a simple rotation of the surface of revolution about its axis, we can obtain any value for θ_1 .

The condition $\sin(\theta_1 - \theta_2) = \sin(\theta_1 - \theta_3) = 0$ can be stated in words as the following: Either all contacts are on the same meridian, or two of them are on the same meridian, and the other is on a meridian displaced 180° from the first.

Since Table 2 gives all the possibilities for correctly matched planes, when considering the intersection of three planes where one or more of the planes is not correctly matched, we need only concern ourselves with the two situations above, namely, case 1 and cases 4 and 5. Any other type of intersection will obviously be the result of

Conditions	Rank A	Rank [A \underline{d}]	Case(s)	Configuration Type
$\sin(\theta_1 - \theta_2) = 0$ and $\sin(\theta_1 - \theta_3) = 0$	1	1	1	Singular
otherwise	2	2	4,5	Nonsingular

Table 2. Possibilities for 3 Correctly Matched Planes

incorrectly matched planes. Consider case 1 first (coincident planes). If this occurs among any of our eight plane labeling combinations, then we have insufficient information to solve for the axis of the surface of revolution. Otherwise, case 4 or 5 will occur at least once, and if it occurs only once, then the axis of the surface of revolution will be the line intersection (see section 2.4.2). However, if a case 4 or 5 intersection (i.e., a line intersection) occurs more than once among the eight combinations, then, again, we have a singular configuration and it is not possible to solve for the axis, although the axis will be one of the multiple line intersections.

Although eight different matchings are possible, we need only look at three separate cases since the subscripts we use to denote parameters associated with particular contacts are arbitrary (i.e., the contact we label as 2 could just as well have been called 1 or 3). The cases we will examine are

1. Planes 1 and 2 correctly matched (i.e., determined by \underline{p} , \hat{n} , and \hat{k}_z); Plane 3 incorrectly matched (i.e., determined by \underline{p} , \hat{n} , and \hat{k}_θ).
2. Plane 1 correctly matched; Planes 2 and 3 incorrectly matched.
3. Planes 1, 2, and 3 incorrectly matched.

First, though, we need to find the equation for an incorrectly matched plane.

3.3. Equation for an Incorrectly Matched Plane

From equation (16) we have (a, b, c) for an incorrectly matched plane since the plane is perpendicular to \hat{k}_z . Since the point of contact (equation (1)) is included in the plane, we can determine d by substitution into the plane equation,

$$ax + by + cz = d . \tag{23}$$

The perpendicular distance from the plane to the origin is therefore

$$d = \frac{r(z)r'(z)+z}{\sqrt{r'^2(z)+1}} = \hat{k}_z \cdot \underline{p}. \quad (42)$$

Multiplying through by the common denominator gives us the equation for an incorrectly matched plane:

$$r'(z)\cos\theta x + r'(z)\sin\theta y + z = r(z)r'(z) + z. \quad (43)$$

3.4. Situation 1: Planes 1 and 2 Correctly Matched; Plane 3 Incorrectly Matched

We have

$$A = \begin{bmatrix} -\sin\theta_1 & \cos\theta_1 & 0 \\ -\sin\theta_2 & \cos\theta_2 & 0 \\ r'(z_3)\cos\theta_3 & r'(z_3)\sin\theta_3 & 1 \end{bmatrix}, \quad \underline{d} = \begin{bmatrix} 0 \\ 0 \\ r(z_3)r'(z_3) + z_3 \end{bmatrix}. \quad (44)$$

By applying Gaussian elimination we obtain the result in Table 3.

Condition	Rank A	Rank [A \underline{d}]	Case
$\sin(\theta_1 - \theta_2) = 0$	2	2	4

Table 3. Singular Configurations for 1 Incorrectly Matched Plane

The condition in Table 3 implies that planes 1 and 2 are the same. Then, plane 3 must intersect planes 1 and 2 in a line since it can be shown that it is not possible for the plane of equation (24) to be parallel to the plane of equation (43).

3.5. Situation 2: Plane 1 Correctly matched; Planes 2 and 3 Incorrectly Matched

Now, we have

$$A = \begin{bmatrix} -\sin\theta_1 & \cos\theta_1 & 0 \\ r'(z_2)\cos\theta_2 & r'(z_2)\sin\theta_2 & 1 \\ r'(z_3)\cos\theta_3 & r'(z_3)\sin\theta_3 & 1 \end{bmatrix}, \quad \underline{d} = \begin{bmatrix} 0 \\ r(z_2)r'(z_2) + z_2 \\ r(z_3)r'(z_3) + z_3 \end{bmatrix}. \quad (45)$$

Applying Gaussian elimination we arrive at the result in Table 4.

Condition 2 in Table 4 requires that the surface normals at contacts 2 and 3 intersect on the surface of revolution axis (see equation (21)). This will automatically occur if contacts 2 and 3 are on the same parallel (since $z_2 = z_3$). Figure 1 shows a situation where the surface normals at two contacts intersect on the axis, but the two contacts are

Conditions	Rank A	Rank [A \underline{d}]	Cases
1: $r'(z_2)\cos(\theta_2 - \theta_1) = r'(z_3)\cos(\theta_3 - \theta_1)$ and 2: $r(z_2)r'(z_2) + z_2 = r(z_3)r'(z_3) + z_3$	2	2	4,5

Table 4. Singular Configurations for 2 Incorrectly Matched Planes

not on the same parallel.

Whether the second condition can be satisfied for contacts not on the same parallel is entirely dependent on the sweeping rule. For a circular cylinder or cone, for example, the only way that the second condition in Table 4 can be satisfied is if contacts 2 and 3 are on the same parallel. Assume that we have two parallels, possibly the same, such that the second condition is satisfied. Then $r'(z_2)$ and $r'(z_3)$ are defined. By rotational symmetry, we can choose $\theta_1 = 0$. Then the first condition becomes

$$r'(z_2)\cos\theta_2 = r'(z_3)\cos\theta_3. \quad (46)$$

If both $r'(z_2)$ and $r'(z_3)$ are zero, then there are no restrictions on θ_2 and θ_3 (i.e., the solution is the entire θ_2 - θ_3 plane). If at least one of $r'(z_2)$ and $r'(z_3)$ is not zero, then there exists a continuum of solutions for (θ_2, θ_3) (i.e., the solution is a set of curves in the θ_2 - θ_3 plane).

3.6. Situation 3: Planes 1, 2, and 3 Incorrectly Matched

For this last case we have

$$\mathbf{A} = \begin{bmatrix} r'(z_1)\cos\theta_1 & r'(z_1)\sin\theta_1 & 1 \\ r'(z_2)\cos\theta_2 & r'(z_2)\sin\theta_2 & 1 \\ r'(z_3)\cos\theta_3 & r'(z_3)\sin\theta_3 & 1 \end{bmatrix}, \quad \underline{d} = \begin{bmatrix} r(z_1)r'(z_1) + z_1 \\ r(z_2)r'(z_2) + z_2 \\ r(z_3)r'(z_3) + z_3 \end{bmatrix}. \quad (47)$$

First, let $r'(z_1) = r'(z_2) = r'(z_3) = 0$. Now, $\text{rank } \mathbf{A} = \text{rank } [\mathbf{A} \quad \underline{d}] = 1$ only if $z_1 = z_2 = z_3$. This corresponds to a case 1 intersection.

Next, let $r'(z_1) \neq 0$. Now, since the upper left element of \mathbf{A} is not 0 we may proceed using Gaussian elimination to obtain conditions for a case 1 and/or a case 4 or 5 intersection which are singular configurations. We obtain

$$[A \underline{d}] \rightarrow \begin{bmatrix} r'(z_1)c_1 & r'(z_1)s_1 & 1 & (\underline{a}_1)_z \\ 0 & r'(z_1)r'(z_2)s_{(1-2)} & r'(z_2)c_2 - r'(z_1)c_1 & r'(z_2)c_2(\underline{a}_1)_z - r'(z_1)c_1(\underline{a}_2)_z \\ 0 & r'(z_1)r'(z_3)s_{(1-3)} & r'(z_3)c_3 - r'(z_1)c_1 & r'(z_3)c_3(\underline{a}_1)_z - r'(z_1)c_1(\underline{a}_3)_z \end{bmatrix}. \quad (48)$$

where we have used

$$\begin{aligned} (\underline{a}_i)_z &= r(z_i)r'(z_i) + z_i, \quad i = 1, 2, 3, \\ c_i &= \cos(\theta_i), \quad s_i = \sin(\theta_i), \quad i = 1, 2, 3, \\ c_{(i-j)} &= \cos(\theta_i - \theta_j), \quad s_{(i-j)} = \sin(\theta_i - \theta_j), \quad i = 1, 2, 3. \end{aligned} \quad (49)$$

Now, for rank $A = \text{rank } [A \underline{d}] = 1$, we must have

$$\sin(\theta_1 - \theta_2) = \sin(\theta_1 - \theta_3) = 0, \quad (50)$$

$$r'(z_1)\cos\theta_1 = r'(z_2)\cos\theta_2 = r'(z_3)\cos\theta_3, \quad (51)$$

and

$$\frac{r'(z_1)\cos\theta_1}{(\underline{a}_1)_z} = \frac{r'(z_2)\cos\theta_2}{(\underline{a}_2)_z} = \frac{r'(z_3)\cos\theta_3}{(\underline{a}_3)_z}. \quad (52)$$

We can assume that $(\underline{a}_i)_z \neq 0$, $i = 1, 2, 3$ since the origin of our object-oriented coordinate system can be chosen to be anywhere on the axis. Notice that combining equation (51) with equation (50) implies

$$r'(z_2) = \pm r'(z_1), \quad r'(z_3) = \pm r'(z_1)$$

Similarly, the combination of equations (52) and (50) allows cancellation of the cosines in equation (52). This is a result of the fact that the surface of revolution is invariant with respect to rotations about its axis, and therefore, conditions cannot depend on θ_1 , θ_2 , and θ_3 separately.

Next, let $r'(z_2)\sin(\theta_1 - \theta_2) = r'(z_3)\sin(\theta_1 - \theta_3) = 0$. The conditions for rank $A = \text{rank } [A \underline{d}] = 2$ are now

$$r'(z_2)\cos\theta_2 \neq r'(z_1)\cos\theta_1 \quad \text{or} \quad r'(z_3)\cos\theta_3 \neq r'(z_1)\cos\theta_1, \quad (53)$$

and

$$r'(z_1)c_1 \left[(\underline{a}_3)_z - (\underline{a}_2)_z \right] + r'(z_2)c_2 \left[(\underline{a}_1)_z - (\underline{a}_3)_z \right] + r'(z_3)c_3 \left[(\underline{a}_2)_z - (\underline{a}_1)_z \right] = 0. \quad (54)$$

Although it appears that these conditions depend on the angles θ_1 , θ_2 , and θ_3 independently, which does not make sense since the surface of revolution is invariant with

respect to rotations about its axis, by examining the individual cases, we see that this is not the case (this is similar to equations (50) - (52), although not quite as obvious). Consider the following situation:

$$r'(z_1) \neq 0, r'(z_2) = 0, \theta_1 = \theta_3. \quad (55)$$

Combining these conditions with those from equations (53) and (54) results only in the condition

$$r'(z_1) \left[(\underline{a}_3)_z - (\underline{a}_2)_z \right] + r'(z_3) \left[(\underline{a}_2)_z - (\underline{a}_1)_z \right] = 0, \quad (56)$$

which does not depend on the angles independently.

Finally, consider the case where $r'(z_2)\sin(\theta_1 - \theta_2) \neq 0$. We can then row reduce one more time to obtain the conditions

$$\frac{1}{r'(z_1)} \sin(\theta_2 - \theta_3) + \frac{1}{r'(z_2)} \sin(\theta_3 - \theta_1) + \frac{1}{r'(z_3)} \sin(\theta_1 - \theta_2) = 0, \quad (57)$$

and

$$\frac{(\underline{a}_1)_z}{r'(z_1)} \sin(\theta_2 - \theta_3) + \frac{(\underline{a}_2)_z}{r'(z_2)} \sin(\theta_3 - \theta_1) + \frac{(\underline{a}_3)_z}{r'(z_3)} \sin(\theta_1 - \theta_2) = 0. \quad (58)$$

A summary for the case of three incorrectly matched planes appears in Table 5.

The first condition for a singular configuration is easy to understand: All three contacts are on the same parallel, and on this parallel, the sweeping rule has its first derivative equal to zero. This clearly gives us three coincident planes. The second condition in Table 5 is already contained in a previous singular configuration and therefore does not add a new type of singular configuration (see Table 2). Also, the third condition is contained in previous singular configurations. If either $\sin(\theta_1 - \theta_2) = 0$ or $\sin(\theta_1 - \theta_3) = 0$ then we have a previously mentioned singular configuration (see Table 3). In order for the second condition to hold and not have $\sin(\theta_1 - \theta_2) = 0$ or $\sin(\theta_1 - \theta_3) = 0$, we must have $r'(z_2) = r'(z_3) = 0$. Substituting this into equation (54) gives us $(\underline{a}_3)_z = (\underline{a}_2)_z$, and the combination of this with $r'(z_2) = r'(z_3) = 0$ is already contained in Table 4. The fourth condition is not contained in any previously mentioned conditions for a singular configuration. We can get an idea of the types of solutions that exist for equations (57) and (58) by considering the intersection of the following surfaces represented by the equations:

$$\frac{1}{r'(z_1)} x + \frac{1}{r'(z_2)} y + \frac{1}{r'(z_3)} z = 0, \quad (59)$$

$$\frac{(\underline{a}_1)_z}{r'(z_1)} x + \frac{(\underline{a}_2)_z}{r'(z_2)} y + \frac{(\underline{a}_3)_z}{r'(z_3)} z = 0, \quad (60)$$

Condition(s)	Rank A	Rank [A \underline{d}]	Case(s)
$r'(z_1) = r'(z_2) = r'(z_3) = 0$ and $z_1 = z_2 = z_3$	1	1	1
$r'(z_1) \neq 0$ and $\sin(\theta_1 - \theta_2) = \sin(\theta_1 - \theta_3) = 0$ and (50) - (52)	1	1	1
$r'(z_1) \neq 0$ and $r'(z_2)\sin(\theta_1 - \theta_2) = r'(z_3)\sin(\theta_1 - \theta_3) = 0$ and (53) and (54)	2	2	4,5
$r'(z_1), r'(z_2), r'(z_3) \neq 0$ and $\sin(\theta_1 - \theta_2) \neq 0$ and (57) and (58)	2	2	4,5

Table 5. Singular Configurations for 3 Incorrectly Matched Planes

and

$$\begin{bmatrix} x \\ y \\ z \end{bmatrix} = \begin{bmatrix} \sin(\theta_2 - \theta_3) \\ \sin(\theta_3 - \theta_1) \\ \sin(\theta_1 - \theta_2) \end{bmatrix} . \quad (61)$$

Equations (59) and (60) are planes which pass through the origin, while equation (61) is a complicated surface. Since the planes represented by equations (59) and (60) have the origin in common, they either intersect in a line, or they are the same plane. Clearly, if

$$(\underline{a}_1)_z = (\underline{a}_2)_z = (\underline{a}_3)_z , \quad (62)$$

then the planes are the same. This can only be true if the normals at all three contacts intersect at the same point on the axis. This can happen, for example, when all three

contacts are on the same parallel. In this situation the intersection of the coincident planes of equations (59) and (60) and the surface defined by equation (61) is typically a curve. This implies that given these conditions, the solution for $(\theta_1 = 0, \theta_2, \theta_3)$ is a curve in the θ_2 - θ_3 plane. If the normals at the three contacts do not intersect at the same point on the axis, the intersection of the planes defined by equations (59) and (60) is a line. The intersection of this line with the surface of equation (61) is typically two points. Under these conditions, the solution for $(\theta_1 = 0, \theta_2, \theta_3)$ is a set of points in the θ_2 - θ_3 plane.

3.7. Umbilical Point

At an umbilical point all directions are principal directions [Lipschutz, 1969] and hence we cannot uniquely determine $\hat{\kappa}_{\theta_1}$ and $\hat{\kappa}_{z_1}$. If any of our contacts is on an umbilical point, therefore, we have a singular configuration since the other two contacts do not provide enough information to determine the axis. The conditions for an umbilical point can be found simply by equating κ_{z_1} to κ_{θ_1} . From equations (19) and (20) we obtain the condition

$$-r(z_1)r''(z_1) = r'^2(z_1) + 1. \quad (63)$$

3.8. Singular Configuration Summary

For an arbitrary set of three contacts, there are three possibilities:

1. Of the eight possible matchings of curvature directions, only one match has rank $A = \text{rank}[A \ d] = 2$, and no match has $A = \text{rank}[A \ d] = 1$. This match, then, determines the axis.
2. Of the eight possible matchings, more than one match has rank $A = \text{rank}[A \ d] = 2$, but no match has rank $A = \text{rank}[A \ d] = 1$. There will be multiple possibilities for the surface of revolution axis; however, the correct axis will be among the possibilities.
3. Of the eight possibilities, at least one match has rank $A = \text{rank}[A \ d] = 1$. Then, we assume that this is the correct matching, and therefore the axis is not determined at all.

Because of the fact that several of the singular configurations given in Tables 2 through 5 are redundant, we include Table 6 which lists all of the unique singular configurations. In words, the types of configurations that prevent us from performing the matching and/or determining the axis are contacts on the same meridian or meridians separated by 180° and contacts on the same parallel or contacts on different parallels

Condition(s)	Rank A	Rank [A \underline{d}]	Case(s)
$r'(z_1) = r'(z_2) = r'(z_3) = 0$ and $z_1 = z_2 = z_3$	1	1	1
$\sin(\theta_1 - \theta_2) = 0$ and $\sin(\theta_1 - \theta_3) = 0$	1	1	1
$\sin(\theta_1 - \theta_2) = 0$	2	2	4,5
$r'(z_2)\cos(\theta_2 - \theta_1) = r'(z_3)\cos(\theta_3 - \theta_1)$ and $r(z_2)r'(z_2) + z_2 = r(z_3)r'(z_3) + z_3$	2	2	4,5
$r'(z_1), r'(z_2), r'(z_3) \neq 0$ and $\sin(\theta_1 - \theta_2) \neq 0$ and (57) and (58)	2	2	4,5
$-r(z_1)r''(z_1) = r'^2(z_1) + 1$ (umbilical point)	—	—	—

Table 6. Summary of Unique Singular Configurations

where the surface normals intersect at the same point on the axis.

4. Error Analysis

By considering the propagation of errors of the sensed tactile parameters

$$\{ \kappa_\theta, \kappa_z, \hat{k}_\theta, \hat{k}_z, \hat{n}, \underline{p} \}$$

through the equations derived in section 2, we can derive bounds on the uncertainty in the calculated position and orientation of the axis. Specifically, we will consider the axis position error, which is defined to be the minimum distance between the true axis and the calculated axis and the axis orientation error, which is the angle between the calculated axis and the true axis. We assume here that we have successfully matched the principal curvature direction and magnitude data (we showed that this is possible for nonsingular

configurations for the curvature direction method in the last section) and therefore need only consider the error propagation as a function of two contacts (This is also much simpler). In comparing the propagation of the errors using the curvature magnitudes versus curvature directions, we need to consider both the magnitude of the resulting axis position and orientation error for typical experimental parameters, as well as the manner in which the magnitude of the error varies as a function of the variables present in experiments.

4.1. Notation

Our notation for this section is summarized in Table 7.

Symbol	Description	Upper Bound
δ	Minimum Axis Position Error	Equation (64)
ϕ	Axis Orientation Error	Equation (71), Equation (72)
$\ \Delta \underline{a}\ $	Axis Position Uncertainty	Equation (68)
$\ \Delta \underline{p}\ $	Contact Position Uncertainty	0.01 in.
$\ \Delta \hat{n}\ $	Surface Normal Uncertainty	$\pm 1^\circ$
$\ \Delta \hat{k}_z\ , \ \Delta \hat{k}_\theta\ $	Curvature Direction Uncertainties	$\pm 2^\circ, \pm 3^\circ$
$\frac{\Delta \rho_\theta}{\rho_\theta}$	Relative Radius Estimate Error	25 %

Table 7. Error Analysis Notation

The values in Table 7 were based on experiments by Fearing and Binford [1988]. Notice that since all three of the direction vectors (i.e., \hat{n} , \hat{k}_θ , and \hat{k}_z) are of unit length, and since the orientation uncertainty can be assumed to be small, the uncertainty angle in radians is approximately equal to the magnitudes of the error vectors. Therefore, we will introduce a slight abuse of notation by expressing the magnitude of the error vectors in degrees (e.g., $\|\Delta \hat{n}\| \frac{180}{\pi}$ is approximately the uncertainty angle of \hat{n} in degrees). Also note that $\rho_\theta (= \frac{1}{\kappa_\theta})$ is different from r (which is the generating curve).

4.2. Axis Uncertainty Using Magnitudes of Curvature

Here we derive approximate bounds on the axis error when it is calculated from the magnitudes of curvature at a pair of points.

4.2.1. Axis Position Error, δ

To determine the axis of a surface of revolution using magnitudes of curvature, two points on the axis are calculated using equation (21). The maximum position error will occur when both measurements are in error by the upper bound on $\|\Delta \underline{a}\|$ and $\Delta \underline{a}_1$ is in the same direction as $\Delta \underline{a}_2$ (see Figure 4).

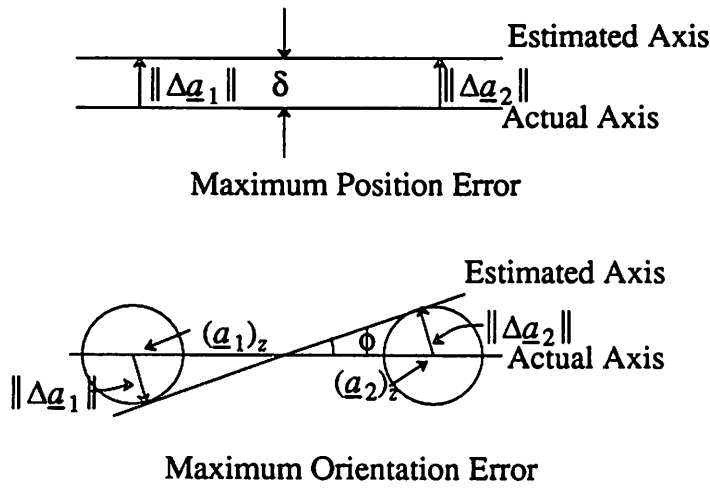


Figure 4. Maximum Position and Orientation Errors

Therefore, we have the result

$$\delta \leq \|\Delta \underline{a}\|. \quad (64)$$

4.2.2. Calculation of $\|\Delta \underline{a}\|$

Recall from equation (21) that a point on the axis is given by

$$\underline{a} = \underline{p} - \rho_{\theta} \hat{n}. \quad (65)$$

Calculating the first-order expansion yields an approximate value for $\|\Delta \underline{a}\|$:

$$\Delta \underline{a} \approx \Delta \underline{p} - \Delta \rho_{\theta} \hat{n} - \rho_{\theta} \Delta \hat{n}. \quad (66)$$

Now, using the triangle inequality twice,

$$\|\underline{x} + \underline{y} - \underline{z}\| \leq \|\underline{x}\| + \|\underline{y}\| + \|\underline{z}\|, \quad (67)$$

we have

$$\|\Delta \underline{a}\| \leq \|\Delta \underline{p}\| + \rho_\theta \left[\frac{\Delta \rho_\theta}{\rho_\theta} + \|\Delta \hat{n}\| \right]. \quad (68)$$

Figure 5 shows a plot of the axis position error for the curvature magnitude method.

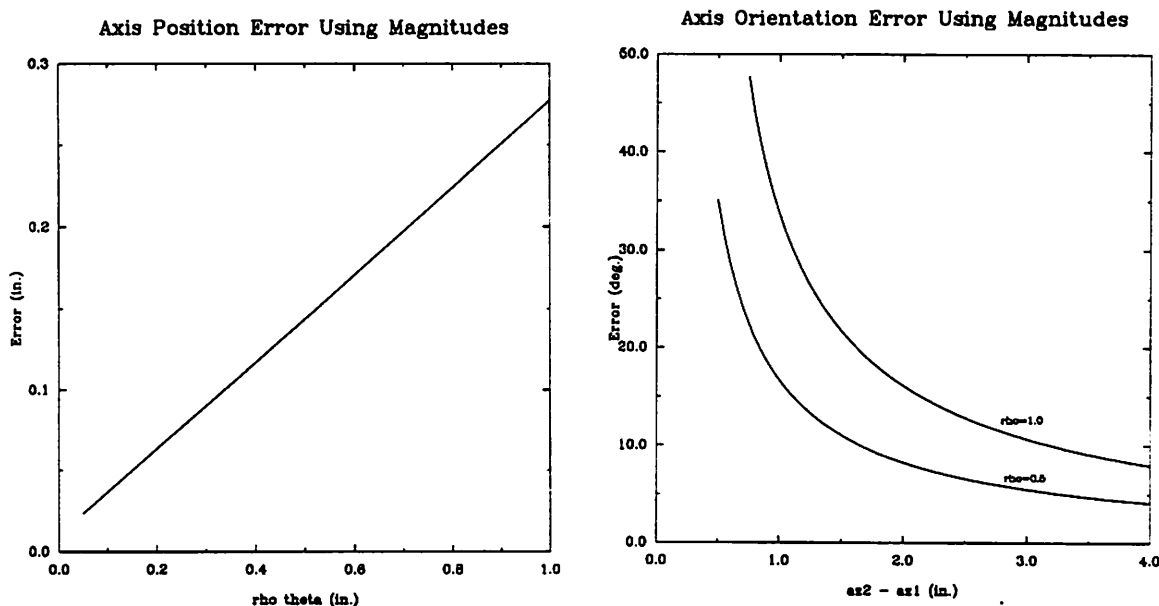


Figure 5. Axis Error Using Curvature Magnitudes

4.2.3. Axis Orientation Error, ϕ

The maximum orientation error occurs when \underline{a}_1 and \underline{a}_2 are anti-parallel (see Figure 4). From equation (21), the distance between the actual two points on the axis, $\underline{p}_1 - \frac{1}{\kappa_{\theta 1}} \hat{n}_1$ and $\underline{p}_2 - \frac{1}{\kappa_{\theta 2}} \hat{n}_2$ is

$$\left| z_2 + r(z_2)r'(z_2) - \left[z_1 + r(z_1)r'(z_1) \right] \right|. \quad (69)$$

Using the simple geometry from Figure 4 and letting

$$(\underline{a}_i)_z = z_i + r(z_i)r'(z_i), \quad i = 1, 2, \quad (70)$$

we have the following result:

$$\phi \leq \sin^{-1} \left[\frac{\|\Delta \underline{a}\|}{\frac{1}{2} |(\underline{a}_2)_z - (\underline{a}_1)_z|} \right]. \quad (71)$$

This agrees with our intuition. From equation (28) we know that if the points calculated on the axis are coincident (i.e., $|(\underline{a}_2)_z - (\underline{a}_1)_z| = 0$), we cannot determine the axis.

Therefore if $|(\underline{a}_2)_z - (\underline{a}_1)_z|$ is small, we would expect that there would be a relatively large possibility for error, and this is exactly what we see in equation (71). In words, when determining the axis from curvature magnitudes, the least amount of orientation error is possible when the points on the axis are as far apart as possible (Recall that these points on the axis are $\frac{1}{\kappa_\theta}$ from the contact point along the surface normal). In Figure 6 contacts 1 and 3 have the least amount of orientation error possible, while contacts 1 and 2 have the most.

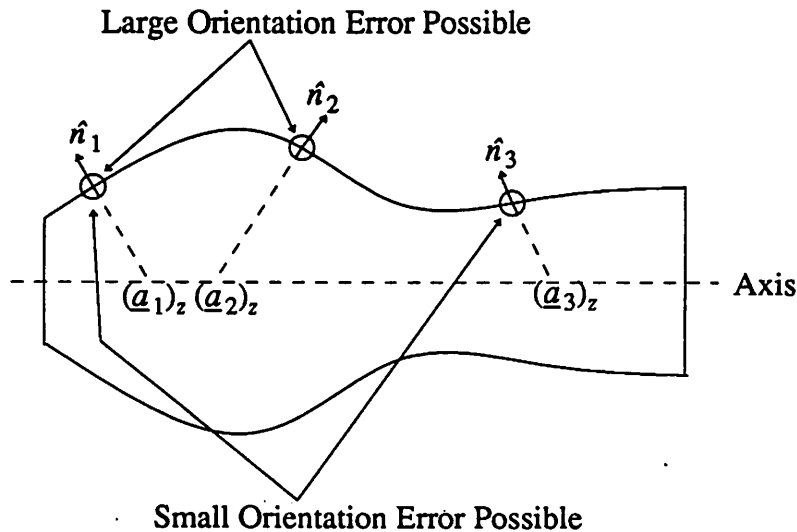


Figure 6. Good and Bad Pairs of Contacts for Determining Orientation

Figure 5 shows the orientation error for the method of axis calculation using curvature magnitudes.

4.3. Axis Uncertainty Using Directions of Curvature

In this subsection we calculate bounds on the axis error using the directions of curvature, instead of the curvature magnitudes.

4.3.1. Axis Position Error, δ

Recall from Section 2 that the axis can be determined by the intersection of the planes at two contacts perpendicular to $\hat{k}_{\theta 1}$ and $\hat{k}_{\theta 2}$. To find an upper bound on the minimum distance between the actual axis and the experimentally determined axis using this method, it is sufficient to examine the cross section plane at the contact where $r(z)$ is largest. By considering the region in the cross section where it is possible for the surface normals to intersect due to the orientation error $\|\Delta \hat{n}\|$ and the contact position error,

$\|\Delta \underline{p}\|$, we can determine the maximum possible error. The geometry is illustrated in Figure 7.

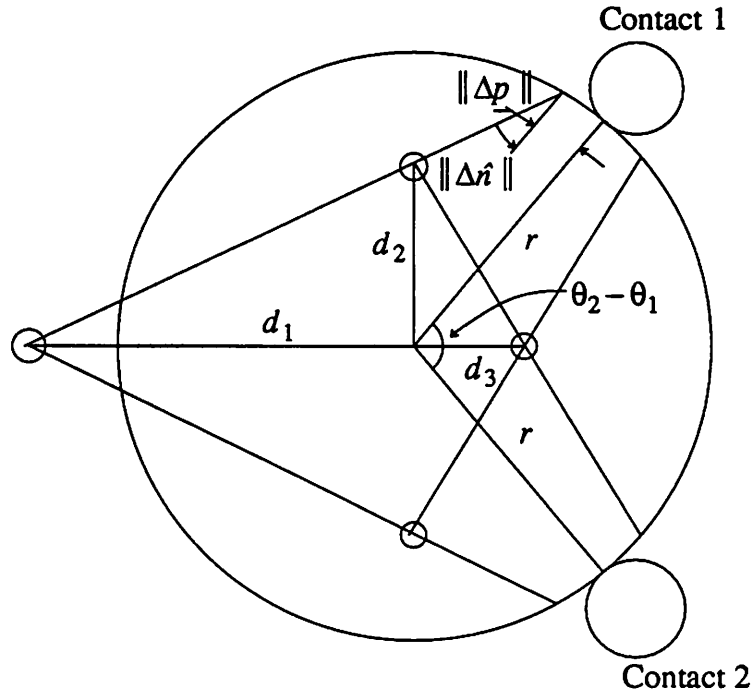


Figure 7. Geometry for Axis Position Error

The small circles mark the vertices of a quadrilateral determined by the angle between the contacts, $\theta_2 - \theta_1$, the surface normal error, $\|\Delta \hat{n}\|$, the contact position error, $\|\Delta \underline{p}\|$, and the radius of the cross section, $r(z)$. Due to the errors, it is possible for the results of experimental data to show that the axis is anywhere within the boundaries of the quadrilateral. Therefore, by computing the distance from the center to the vertex that is the furthest away, we obtain bounds on the position error of the axis determined from experimental data. We can see that a bad situation is $\theta_2 - \theta_1$ small, for then, d_1 can become arbitrarily large. As $\theta_2 - \theta_1$ increases, d_1 becomes shorter; however, d_2 increases. At approximately $\theta_2 - \theta_1 = 90^\circ$, d_2 becomes longer than d_1 and will continue to increase without bound until $\theta_2 - \theta_1 = 180^\circ$. This agrees with the singular configuration of Table 2. Figure 8 contains a plot of δ .

4.3.2. Axis Orientation Error, ϕ

Recall that the orientation of the axis is computed from the cross product

$$\hat{k}_{\theta_1} \times \hat{k}_{\theta_2}.$$

(see equation (31)). Ellis [1989] has determined the bound on this error by using the

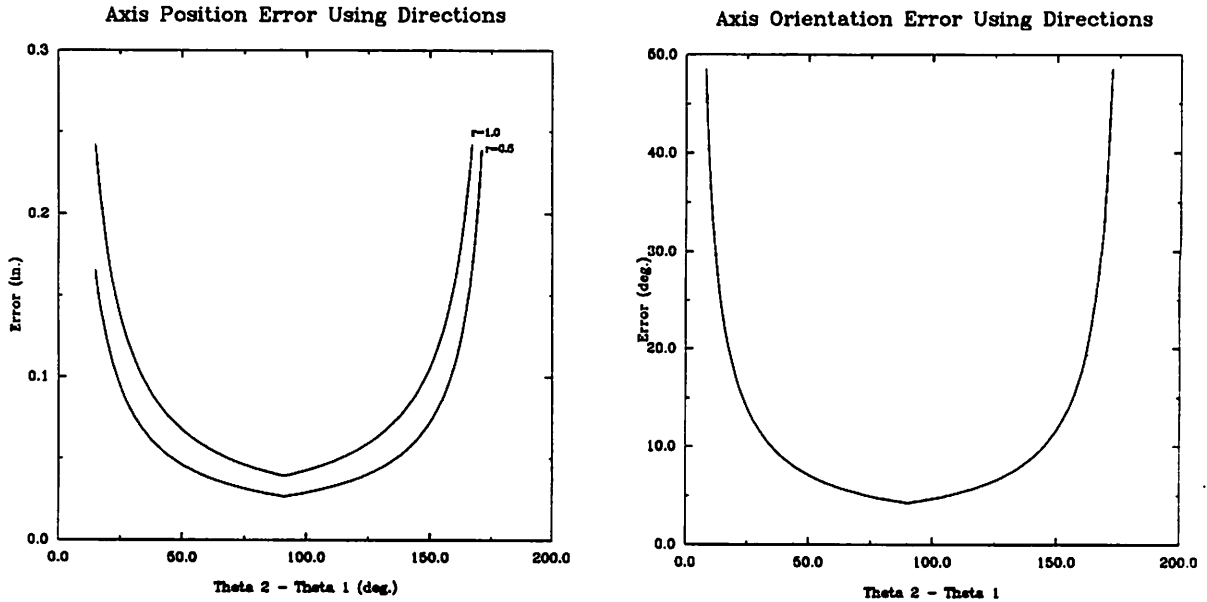


Figure 8. Axis Error Using Curvature Directions

Gaussian sphere, which we use here. \hat{k}_{θ_1} and \hat{k}_{θ_2} become points on the Gaussian sphere. The set of vectors perpendicular to \hat{k}_{θ_1} is a great circle, as is the set of vectors perpendicular to \hat{k}_{θ_2} . Their cross product is then represented by the intersection of these two great circles. When there is uncertainty in \hat{k}_{θ_1} and \hat{k}_{θ_2} , the points representing the vectors become small circles on the sphere, while the great circles become bands of uncertainty. The intersection of the two bands is a curvilinear rhombus (see Figure 9). From Ellis [1989] the uncertainty is given by

$$\phi \leq \sin^{-1} \left[\frac{\sin \|\Delta \hat{k}_{\theta}\|}{\sin[(\theta_2 - \theta_1)/2]} \right] \quad (72)$$

This is plotted in Figure 8. Note that, similar to the position error in the section above, the minimum error sensitivity occurs when the contacts are 90° apart.

5. Experimental Results

Experiments were performed on a RobotWorld system built by Automatrix. This system consisted of suspended modules with x , y , z , and θ degrees of freedom. Our test object was a wooden surface of revolution cut on a lathe with a sweeping rule modeled by a second-degree polynomial. The object was bolted to the ROBOTWORLD work surface at an angle, and a module equipped with the tactile sensor was commanded to probe the object at various locations (see Figure 10).

Recall from section 3 that if the contacts do not form a singular configuration, the three planes defined by \underline{p} , \hat{k}_z , and \hat{n} at each contact intersect in a line, and rank A = rank

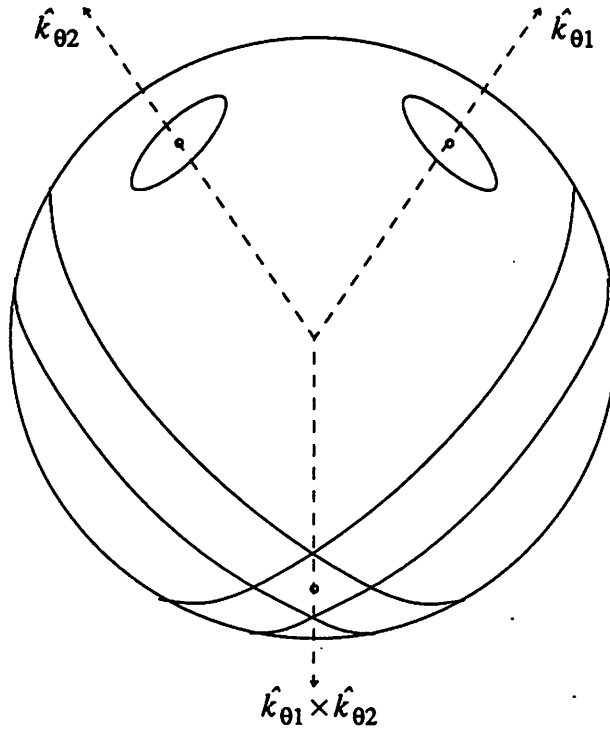


Figure 9. Gaussian Sphere for Cross-Product Error

$[A \ d] = 2$. However, this assumes we have perfect data. With experimental errors, the planes will usually intersect in a point instead of a line, and thus we will have $\text{rank } A = \text{rank } [A \ d] = 3$. This problem can be solved by calculating the singular values of A and $[A \ d]$. The number of singular values greater than a preset tolerance then determines the rank. Now, the three correctly matched planes form a pyramid with the intersection point being the apex, and the three planes being the side faces. The estimated axis is then defined by the point at the apex and the point which is the centroid of the pyramid's base (see Figure 11).

5.1. Preliminary Experiment

The preliminary experiment serves to illustrate our method. Table 7 includes results for the three contacts and the axis determined by these contacts. Figures 11 and 12 show the planes and curvature directions for the experiment. The position and curvature information derived was sufficient to determine the axis using a tolerance for singular value decomposition of 0.1. However, these contacts were chosen carefully to avoid singular configurations. A more comprehensive set of experiments were performed to examine the effects of contacts close to singular configurations.

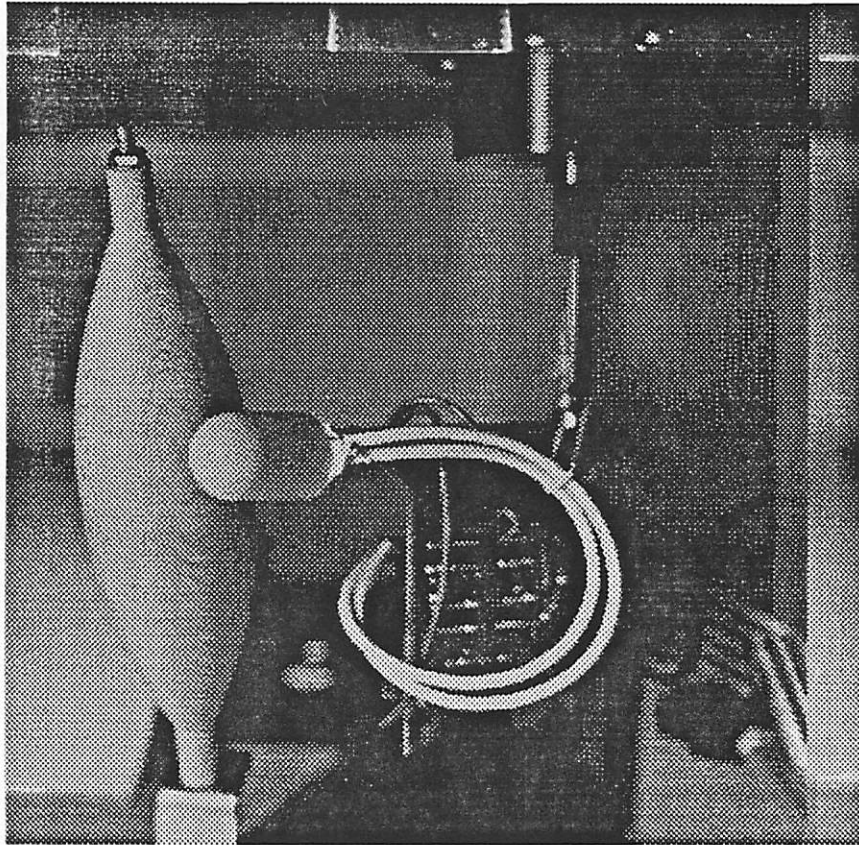


Figure 10. RobotWorld Experimental Set-Up

5.2. Comprehensive Experiment

Table 8 shows the curvature information and positions derived from 12 contacts. The curvature information for contacts 9 and 10 was badly corrupted. Contacts 11 and 12 were taken at approximately the same point as contact 10 in an attempt to improve the results. Contact 12 had the best overall result of these 3, and so it was used to represent this position on the object. Notice that groups (1,2,3), (4,5,6), (7,8), and (9,12) have close to the same value for θ . Thus, configurations containing two contacts from any one group will be close to singular.

Given 10 contacts, there are 120 different combinations of 3 contact groups. When tested with tolerances of 0.005, 0.01, and 0.05, very few of the combinations were nonsingular. Of those which were nonsingular, many gave a false axis. This poor performance can be attributed to the relatively large orientation errors, the gradual sweeping rule of our object ($r'(z)$ close to zero), and similar values for θ for several groups of contacts. Figure 13 shows the results of the experiments. Note that there tend to be clusters around 0° angle error and around 100° angle error. The cluster around 100° was due to wrongly matched planes (which were almost perpendicular to axis) intersecting correctly matched planes. For those combinations which gave the correct axis, the angle error was

Feature	Vector	Estimate	Actual	Error
Axis	Position Direction	[35.35 26.04 2.83] [-.29 .06 .95]	[35.32 26.1 2.82] [-.40 0 .92]	.07 in. 7.3°
Contact 1 $\theta = 283.7^\circ$ $z = 4.35$ in.	\underline{p} \hat{k}_z \hat{k}_θ	[35.64 25.12 2.69] [.28 -.17 -.95] [-.94 -.26 -.23]	[35.63 25.19 2.68] [.43 -.15 -.89] [-.89 -.23 -.39]	.07 in. 8.7° 9.4°
Contact 2 $\theta = 338.5^\circ$ $z = 4.47$ in.	\underline{p} \hat{k}_z \hat{k}_θ	[36.18 25.76 3.04] [.54 -.12 -.84] [-.31 -.95 -.06]	[36.16 25.76 3.04] [.54 -.06 -.84] [-.34 -.93 -.15]	.01 in. 3.0° 5.2°
Contact 3 $\theta = 25.9^\circ$ $z = 5.13$ in.	\underline{p} \hat{k}_z \hat{k}_θ	[35.72 26.42 3.55] [.59 .10 -.80] [.46 -.86 .23]	[35.76 26.44 3.58] [.60 .11 -.79] [.40 -.90 .17]	.05 in. .8° 4.9°

Table 7. Preliminary Experimental Results

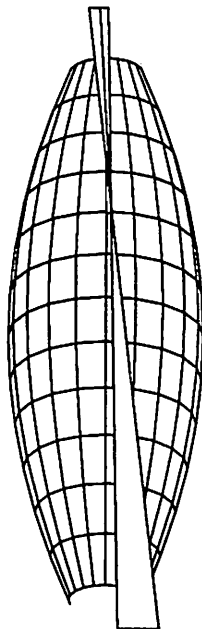


Figure 11. Experimental Planes

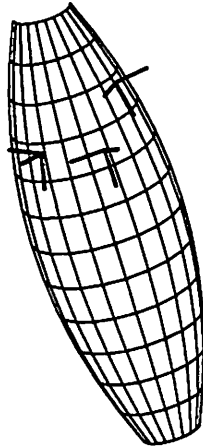


Figure 12. Experimental Curvature Directions

usually below 10° and the position error below 0.3 in. Also, notice the apparent trend: As the tolerance was decreased, the number of nonsingular combinations went down; however, the ratio of correct matches to incorrect matches went up.

Error in our experiments was greater than in Fearing and Binford [1988]. Some of this error can be attributed to imprecise fixtures. Most of the equipment was "home made," and we believe this could cause errors up to a few degrees.

Another source of error was in the manner forces were applied to the sensor. Our current model for the sensor assumes that forces are applied normally to the sensor's surface. Unfortunately, with our RobotWorld system, this was not the case since the motions were position controlled rather than force controlled. One possible solution is to subtract off the odd portion of the strain response. Fearing, Rise, and Binford [1986] showed that the odd portion of the strain response was due to the tangential force, while the even portion was due to the normal force. See the appendix for a more complete error discussion.

6. Conclusions

In general, three contacts with a tactile sensor are sufficient to determine an arbitrary surface of revolution's orientation and location. However, singular configurations exist which can prevent the axis from being determined uniquely, or possibly, from being determined at all. Basically, these involve contacts on the same meridian or meridians separated by 180° and contacts on the same parallel or contacts on different parallels where the surface normals intersect at the same point on the axis.

The bounds on the orientation and position error were calculated as a function of parameters for two contacts. Optimal angular spacing for the curvature direction method

		p (in.)	\hat{n}	\hat{k}_z	\hat{k}_θ	ρ_z (in.)	ρ_θ (in.)
Contact 1 $\theta=99.4^\circ$ $z=5.58$ in.	Est.	[35.19 25.36 2.76]	[-.28 -.95 .14]	[-.44 .26 .86]	[.85 -.18 .49]	6000	.71
	Act.	[35.16 25.28 2.78]	[-.24 -.96 .14]	[-.35 .22 .91]	[.91 -.16 .39]	7.4	.86
	Err.	.09	2.7°	5.8°	6.2°	—	17 %
Contact 2 $\theta=95.6^\circ$ $z=6.07$ in.	Est.	[35.05 25.45 3.23]	[-.26 -.94 .20]	[-.44 .30 .85]	[.86 -.13 .50]	15000	.63
	Act.	[35.04 25.40 3.25]	[-.20 -.95 .23]	[-.35 .29 .89]	[.91 -.10 .40]	7.8	.74
	Err.	.05	3.9°	5.7°	6.9°	—	15 %
Contact 3 $\theta=90.2^\circ$ $z=6.5$ in.	Est.	[34.92 25.62 3.69]	[-.22 -.93 .30]	[-.46 .36 .81]	[.86 -.05 .51]	16000	.43
	Act.	[34.91 25.56 3.71]	[-.14 -.94 .32]	[-.37 .35 .86]	[.92 0.0 .40]	8.3	.58
	Err.	.07	5.0°	5.7°	7.5°	—	25 %
Contact 4 $\theta=14.6^\circ$ $z=4.93$ in.	Est.	[36.41 25.86 2.61]	[.84 -.31 .45]	[-.49 -.05 .87]	[.24 .95 .19]	16000	1.1
	Act.	[36.40 25.86 2.60]	[.83 -.25 .50]	[-.51 .03 .86]	[.23 .97 .10]	7.0	.96
	Err.	.01	4.4°	4.9°	5.2°	—	15 %
Contact 5 $\theta=11.7^\circ$ $z=6.00$ in.	Est.	[35.80 25.95 3.52]	[.76 -.18 .63]	[-.64 -.03 .77]	[.12 .98 .14]	16000	.80
	Act.	[35.77 25.95 3.50]	[.75 -.19 .63]	[-.63 .06 .77]	[.19 .98 .08]	7.8	.75
	Err.	.04	1.2°	5.0°	5.1°	—	6 %
Contact 6 $\theta=10.7^\circ$ $z=5.45$ in.	Est.	[36.16 25.93 3.07]	[.81 -.25 .53]	[-.57 -.14 .81]	[.13 .96 .25]	17000	.90
	Act.	[36.12 25.94 3.04]	[.80 -.18 .57]	[-.57 .04 .82]	[.17 .98 .07]	7.3	.88
	Err.	.04	4.4°	10.2°	10.8°	—	2 %
Contact 7 $\theta=46.0^\circ$ $z=5.34$ in.	Est.	[35.99 26.78 2.88]	[.54 .73 .41]	[-.40 -.21 .89]	[-.74 .65 -.18]	14000	1.25
	Act.	[35.95 26.74 2.85]	[.55 .71 .45]	[-.51 -.14 .85]	[-.66 .70 -.29]	7.3	.90
	Err.	.06	2.6°	8.2°	8.2°	—	39 %
Contact 8 $\theta=46.6^\circ$ $z=5.89$ in.	Est.	[35.69 26.70 3.35]	[.49 .73 .47]	[-.46 -.24 .86]	[-.74 .64 -.22]	14000	1.1
	Act.	[35.65 26.65 3.31]	[.50 .70 .51]	[-.55 -.19 .81]	[-.67 .69 -.29]	7.6	.79
	Err.	.07	2.9°	6.4°	6.5°	—	36 %
Contact 9 $\theta=69.3^\circ$ $z=5.53$ in.	Est.	[35.60 26.96 2.93]	[.19 .93 .31]	[-.23 -.26 .94]	[-.95 .25 -.17]	12000	1.3
	Act.	[35.59 26.89 2.9]	[.23 .91 .34]	[-.46 -.20 .87]	[-.86 .35 -.37]	7.4	.87
	Err.	.08	2.9°	13.9°	14.2°	—	55 %
Contact 10 $\theta=70.6^\circ$ $z=5.05$ in.	Est.	[35.80 27.04 2.48]	[.21 .95 .21]	[-.23 -.16 .96]	[-.95 .25 -.18]	10000	1.3
	Act.	[35.79 26.98 2.46]	[.24 .93 .27]	[-.44 -.14 .89]	[-.87 .33 -.37]	7.1	.95
	Err.	.06	3.9°	13.0°	13.0°	—	41 %
Contact 11 $\theta=71.2^\circ$ $z=5.05$ in.	Est.	[35.80 27.04 2.47]	[.21 .95 .22]	[-.27 -.16 .95]	[-.94 .26 -.22]	10000	1.3
	Act.	[35.78 26.99 2.46]	[.23 .94 .27]	[-.44 -.14 .89]	[-.87 .32 -.38]	7.1	.95
	Err.	.06	3.0°	10.4°	10.4°	—	37 %
Contact 12 $\theta=71.2^\circ$ $z=5.05$ in.	Est.	[35.79 27.04 2.47]	[.21 .95 .22]	[-.29 -.15 .95]	[-.93 .26 -.24]	11000	1.27
	Act.	[35.78 26.99 2.46]	[.23 .94 .26]	[-.44 -.14 .89]	[-.87 .32 -.38]	7.1	.95
	Err.	.06	3.0°	9.2°	9.3°	—	34 %

Table 8. Contacts for Comprehensive Experiment

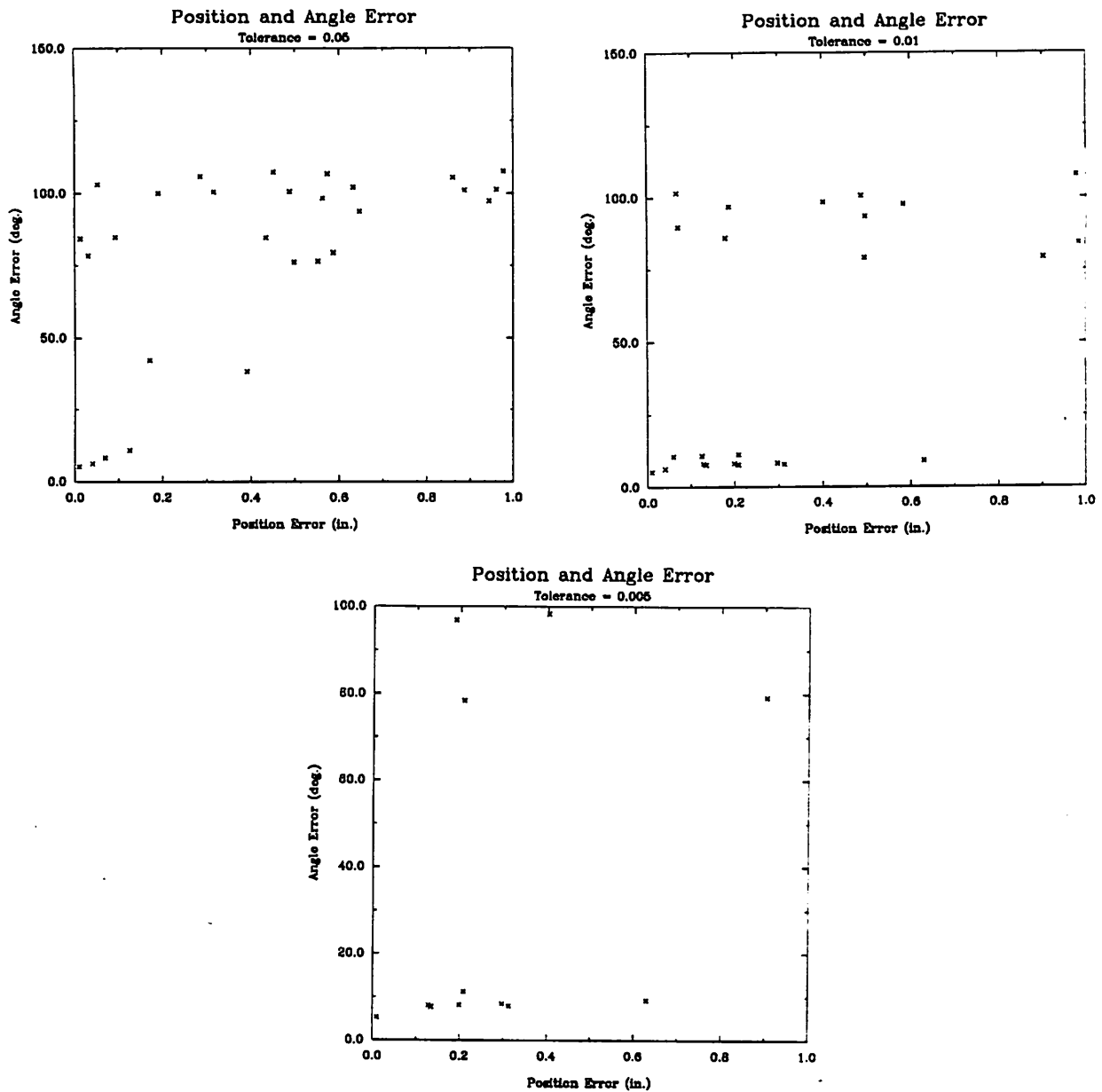


Figure 13. Comprehensive Experimental Results

was seen to be 90° , whereas for the magnitude method, a small ρ_θ and contacts which were far apart produced the smallest error bound. Experiments showed that our method indeed worked for many cases, even in the presence of significant error. Angle error was usually less than 10° and position error less than 0.3 in.

Acknowledgments

We would like to thank Richard M. Murray and Jean Ponce for several helpful discussions and Ed Nicolson for a faster converging curvature estimation program. This work was supported in part by NSF grant IRI-8810585, whose support is gratefully acknowledged.

7. Appendix - Notes on the Curvature from Strain Problem

Fearing and Binford [1988] described the algorithm which is used to determine curvature information from the strain response of the sensor. Here we describe the algorithm's theoretical performance when determining 1 curvature (object is a cylinder) versus determining 2 curvatures (e.g., our surface of revolution). Specifically, we are interested in the reliability of the angle estimate given some amount of sensor noise. The angle, of course, was what was used in the surface of revolution axis finding experiments (Note that Fearing and Binford [1988] used the angle estimates from only the 1 curvature algorithm). We also describe attempts to improve the model for the sensor. Finally, we consider the errors which occurred in our surface of revolution experiments (see section 5).

7.1. Sensitivity to Error

We use the strain response of 16 tactels (4×4 window) for the algorithm. Thus, the sensor error can be written as

$$\Delta \underline{\epsilon}_z = \left[\Delta \epsilon_{z11}, \Delta \epsilon_{z12}, \dots, \Delta \epsilon_{z43}, \Delta \epsilon_{z44} \right]^T . \quad (73)$$

For the algorithm which determines only one curvature, the parameter estimation error is

$$\Delta \underline{R} = \begin{bmatrix} \Delta R_1 \\ \Delta \psi \\ \Delta F \end{bmatrix} , \quad (74)$$

while for the two-curvature algorithm, the error is

$$\Delta \underline{R} = \begin{bmatrix} \Delta R_1 \\ \Delta R_2 \\ \Delta \psi \\ \Delta F \end{bmatrix} . \quad (75)$$

It is desired to find the relation between $\max \Delta \underline{R}$, the maximum expected error in the radii, force, and orientation estimates as a function of $\max \Delta \underline{\epsilon}_z$, the worst case variation in strain sensor measurements. The measured normal strain is represented as a vector function \underline{f}

$$\underline{\epsilon}_{zo} = \underline{f}(R_o, \psi_o, F_o) , \quad (76)$$

where R_o could be either R_{1o} or R_{1o}, R_{2o} . For small strain errors, \underline{f} is expanded in a Taylor's series up to first order about nominal values

$$\underline{\epsilon}_z \approx \underline{\epsilon}_{z0} + \Delta\underline{\epsilon}_z = \underline{\epsilon}_{z0} + \mathbf{J} \begin{bmatrix} \Delta R \\ \Delta \psi \\ \Delta F \end{bmatrix}, \quad (77)$$

where \mathbf{J} is the Jacobian of f . The least-squares matrix solution for $\Delta\underline{R}$ is

$$\Delta\underline{R} = (\mathbf{J}^T \mathbf{J})^{-1} \mathbf{J}^T \Delta\underline{\epsilon}_z = \mathbf{A} \Delta\underline{\epsilon}_z, \quad (78)$$

where the matrix \mathbf{A} is an abbreviated notation for the least-squares inverse. The maximum parameter change in each element of $\Delta\underline{R}$ will occur when $\Delta\underline{\epsilon}_z$ is aligned with \underline{A}_i^T . For example,

$$\max \Delta R_1 = \underline{A}_1^T \Delta\underline{\epsilon}_z = \underline{A}_1^T \frac{\underline{A}_1}{|\underline{A}_1|} |\Delta\underline{\epsilon}_z| = |\underline{A}_1| |\Delta\underline{\epsilon}_z|. \quad (79)$$

The sensor noise due to quantization is [Fearing and Binford, 1988]

$$|\Delta\underline{\epsilon}_z| = 4 (0.05)\% . \quad (80)$$

Figure 14 shows the results for this value of sensor noise. For the one curvature algorithm we used 1 inch for the radius. For the two curvature plot we used radii of 1 and 7 inches. These two radii are close to those for our surface of revolution. The model used for the impulse response was the same as used by Fearing and Binford [1988] except for small parameter changes. Notice the large error sensitivity for the two curvature algorithm. This is because we are trying to obtain more information from the same amount of data. For the axis finding experiments the object angle was in the -25° to 25° range. Thus, an upper bound on the angle error would be 20.5° , not 2° as was assumed in the Error Analysis section. These plots provide a comparison between the two algorithms; however, they do not necessarily predict the actual error that would be encountered. First of all, we assumed a uniform distribution of noise due to quantization and plotted the sensitivity due to the upper bound on the noise. In practice, it would be quite unlikely that the noise would be at this maximum and that it would also be in such a direction so as to produce the value shown in the plot.

7.2. Model Improvements

For strains up to 15%, or so, the sensor is approximately linear. We may also hope the sensor is position-invariant, and thus the sensor can be characterized by its impulse response as a function of position. In an attempt to improve the performance of the sensor we have tried several new impulse response models. We also consider a simple modification to the elasticity model.

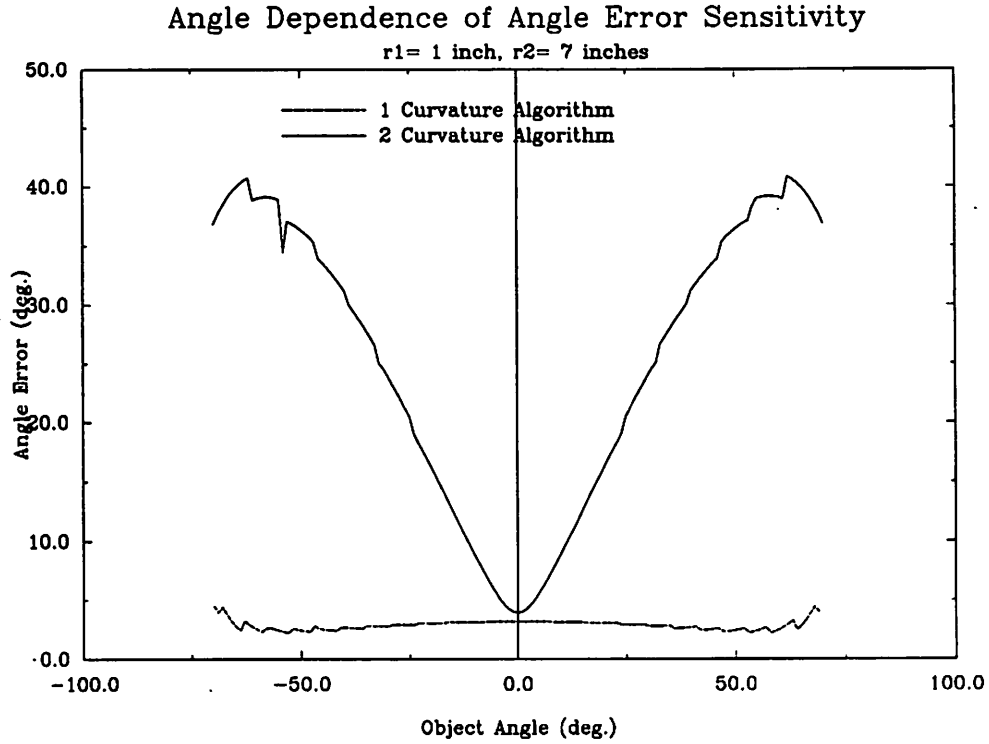


Figure 14. Angle Error Sensitivity

7.2.1. Improved Probing Technique

In Fearing and Binford [1988] the impulse response was determined by probing the sensor with a force balance by hand. This technique limited the number of probes, due to operator fatigue, to about 150 or so. Also, since the probe was dropped by hand, the momentum of the probe striking the sensor was probably different for each contact. The same RobotWorld used to probe our surface of revolution was set up to apply impulse probes to a tactile sensor. Thus we were able to cover the whole surface of the sensor (about 3500 probes) in a consistent manner.

7.2.2. Adding More Parameters

Fearing and Binford [1988] used the following separable model for the impulse response model:

$$h(x,y) = h_x(x) h_y(y) \tag{81}$$

where

$$h_x(x) = \frac{d_x^2(d_x^2 - v_x x^2)}{(x^2 + d_x^2)^2}, \quad h_y(y) = \frac{d_y^2(d_y^2 - v_y y^2)}{(y^2 + d_y^2)^2} \tag{82}$$

d_x, d_y and ν_x, ν_y are depth and Poisson's ratio parameters along the cylinder axis and around the circumference respectively. Each tactel was assumed to have the same values for the different parameters. They also assumed the tactels were positioned uniformly at intervals of 3.3 mm along the axis and 18° around the axis. The first attempt we made to improve the model was to allow each tactel to have its own parameters. This is much more realistic since the sensor was made by hand with relatively large tolerances. Next, we got rid of the uniform spacing assumption by adding x and y position parameters for each element. Fitting the data from the RobotWorld probing measurements and then plotting the positions showed us that the bands were not laid down perfectly straight. For this reason we next added rotation parameters to allow the x and y directions to be altered independently for each tactel:

$$\begin{aligned}x &\rightarrow x \cos(\phi_x) - y \sin(\phi_y) \\ &\text{and} \\ y &\rightarrow y \cos(\phi_y) + x \sin(\phi_x).\end{aligned}\tag{83}$$

The last parameter we added to the models was to allow the shape of the response in the y direction (around axis) to be unsymmetric (Plots of the data showed the shape was roughly symmetric in the x direction but unsymmetric in the y direction.) This was done with

$$h_y(y) \rightarrow (1 + \alpha y)h_y(y).\tag{84}$$

The result of our new model was a fit to the RobotWorld data of about 1-2% of full scale rms.

7.2.3. Deconvolution of Impulse Data

The probe used in producing the impulse response was, of course, not a real impulse. It had a finite width and amplitude. Thus, our next attempt at improving the model was to deconvolve the RobotWorld data with the probe response. This had the expected effect: the shape of the impulse response became slightly sharper and the amplitude increased. Reversing the process and convolving our new model with the probe response gave a slightly better fit to the RobotWorld data than the previous model. The ability of the new model to predict curvature magnitudes and directions was not significantly better than the previous model, however.

7.2.4. Linear Interpolation on Impulse Data

Since the separable model described above had no real theoretical justification, and since the data from the RobotWorld experiment was quite dense (samples were taken at 0.02 inch spacing along the axis and 3° around the axis), it made sense to try to use the data as a direct look-up table. Our first attempt used a 0-order interpolation between samples. Thus, the value for the impulse response as a function of an arbitrary position was taken to be the response of the closest location where a measurement was taken. This did not work well with our fitting program, presumably because the gradient search routine could not handle the discontinuity of the model with respect to position. Next, we tried linear interpolation on the RobotWorld data. This impulse response model behaved almost identically to the complicated models discussed in the previous subsections when determining curvature magnitudes and directions. We chose to work with linear interpolation scheme due to its simplicity.

After improving the impulse response model, we considered a simple change to the elasticity model of the sensor as described in the next subsection.

7.2.5. Increasing the Modulus of Elasticity Parameter

The half space model used in Fearing and Binford [1988] was only an approximation. In their work the modulus of elasticity was determined by a crude measurement on a thick cube of the same type of rubber used in making the tactile finger. They used a value of $2.5 \times 10^5 \text{ N-m}^{-2}$. However, Gobel [1974] includes another approximate model (the bonded spring) in which the modulus of elasticity is replaced by an effective modulus which turns out to be larger. This is due to the fact that the rubber is "bonded" to the surface of the indenter above and to a hard substrate below. This agrees with a simple experiment: the thick cube of rubber feels much softer than the tactile sensor. By trial and error, we found that a value of $4.0 \times 10^5 \text{ N-m}^{-2}$ gave more accurate curvature predictions.

Figure 15 shows a plot of the angle estimated by the 2 curvature algorithm for various angles of a 0.5 inch cylinder contacting the sensor. The plot for $E = 2.5 \times 10^5 \text{ N-m}^{-2}$ shows a consistent error in that a line fit to its points has a slope of 0.79 instead of 1. However, the plot for $E = 4.0 \times 10^5 \text{ N-m}^{-2}$ has a slope of 0.99. The intercept (2° for the $E = 2.5 \times 10^5$ case, 2.5° for the $E = 4.0 \times 10^5$ case) on the Estimated Angle axis was not a concern since on our setup the absolute angle was uncertain while the relative angle was precise.

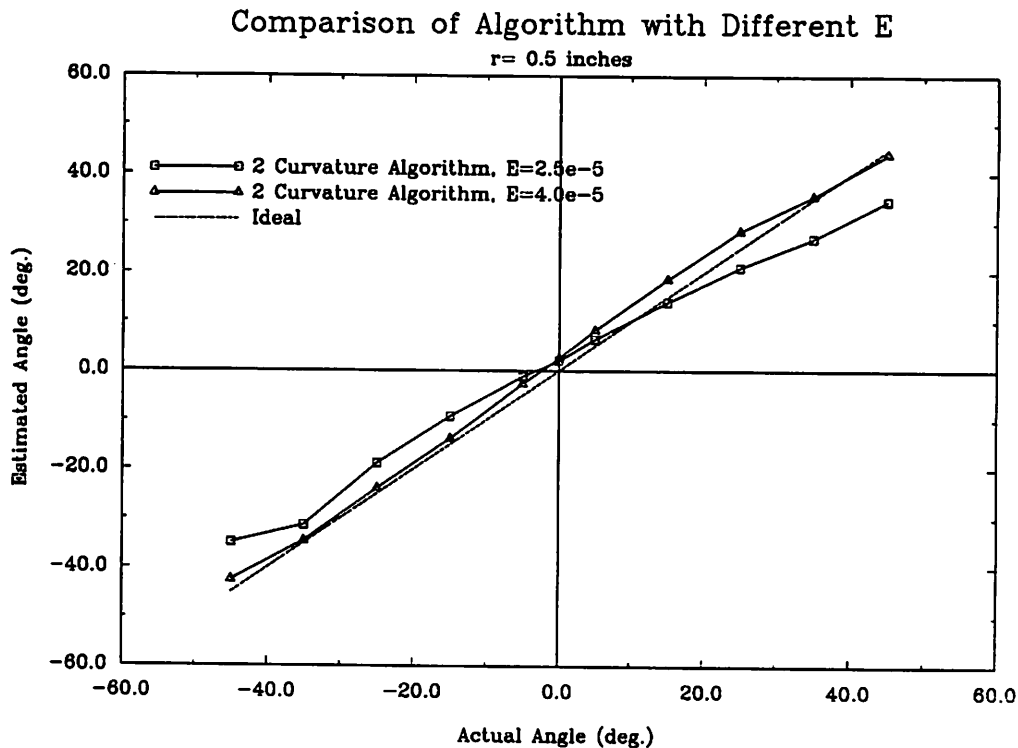


Figure 15. Curvature Algorithm Performance Dependence on E

7.2.6. Remaining Problems

Despite our attempts to improve the model for the sensor, there still are significant problems to be solved.

The curvature algorithm using the linear interpolation on RobotWorld data and a larger modulus of elasticity parameter worked quite well at determining curvature directions, however, there appeared at times an offset of as much as 10° in the estimated angle. This was consistent, however, for a given set up, and all angles measured would exhibit the same offset (see Figure 17). It was at first thought that the offset was due to large tolerances in our testing apparatus. However, this theory could not be justified.

Another problem was the fact that the sensor exhibited highly position-dependent behavior (e.g., the estimated angle of an object with respect to the sensor depended on where the object touched the sensor). The change in the estimated angle was as much as 12° in some cases as we varied the contact location. Thus, it was necessary to take all measurements at a specific location on the sensor. Unfortunately, position-independent behavior is necessary in order for the sensor's response to be characterized by its impulse response. The presence of copper bands beneath the surface of the rubber is one possibility for the position-dependent behavior. This could cause the effective modulus of

elasticity (see Section 7.2.5) to be larger near copper bands since the rubber might be adhering to the bands. Other possibilities include a nonuniform rubber thickness and nonuniform frictional properties of the outside surface of the sensor.

One likely source of error was in the approximations and assumptions we made in our model for the sensor. For simplicity, the half space model (Figure 16A) was used. However, there were different ways that the half space model could be applied to a cylindrical tactile sensor. Basically, these affected how distance in the circumferential direction was calculated and how the impulse probing was done. The first method we considered was that shown in Figure 16B. Here we assumed that the curvature of the finger was small enough so that the finger was like a plane. With this assumption, we had to probe the sensor for its impulse response by parallel probes which were normal to the sensor at a particular line along the finger axis. Distances in the circumferential direction from this line would then be computed as $r \sin(\theta)$ where θ was the angular displacement from the line. The main disadvantage of this assumption was that all contacts had to be made in the vicinity of the line where normal probing occurred. The other method was to assume normal forces as is shown in Figure 16C. Thus we assumed that the half space was "wrapped around" an axis. For this assumption, we probed the sensor normal to its surface. Distances in the circumferential direction from some line along the axis were calculated as $r \theta$ where θ was the angular displacement from the line. We chose this method since the model was valid all over the finger and not just in a small region. Since the contact areas were small (e.g., major and minor axes of the contact ellipse were around 2-4 mm for our surface of revolution), we were able to obtain decent performance from the sensor with our approximation. Although the difference between the vertical force and normal force methods may seem small for these dimensions (e.g., $r = 12.7$ mm, $\theta = 13.7^\circ$ gives $r \sin(\theta) = 3.01$ mm, $r \theta = 3.04$ mm), it was found that the curvature estimation algorithm was extremely sensitive to differences of this order.

As evidence of some problems with our model, impulses (for which the curvature estimation algorithm should return two radii of zero and an exact force estimate) did not fit perfectly. Radii for impulses were in the 0-1 mm range, and forces were estimated too high. The rms fit was in the range of 1-3% of full scale. Perhaps finite element modelling techniques could be used to understand how the use of the half space model for a cylindrical tactile sensor affects the estimated strains. As a first attempt, we might see what effect the curved geometry of the sensor has. Next, the effect of including copper bands beneath the rubber's surface could be simulated.

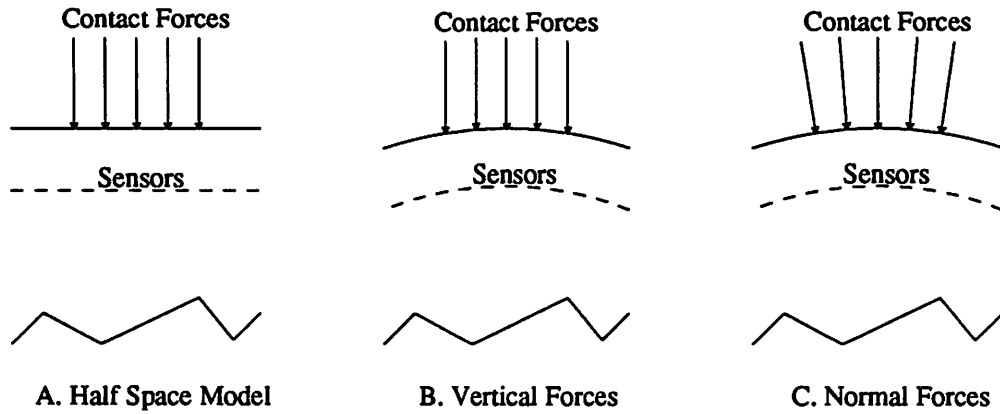


Figure 16. Contact Forces and Elasticity Models

7.3. Surface of Revolution Experimental Errors

Figure 17 shows a plot of both the experimental and ideal angles returned by the curvature estimation algorithm for the surface of revolution data shown in Table 8.

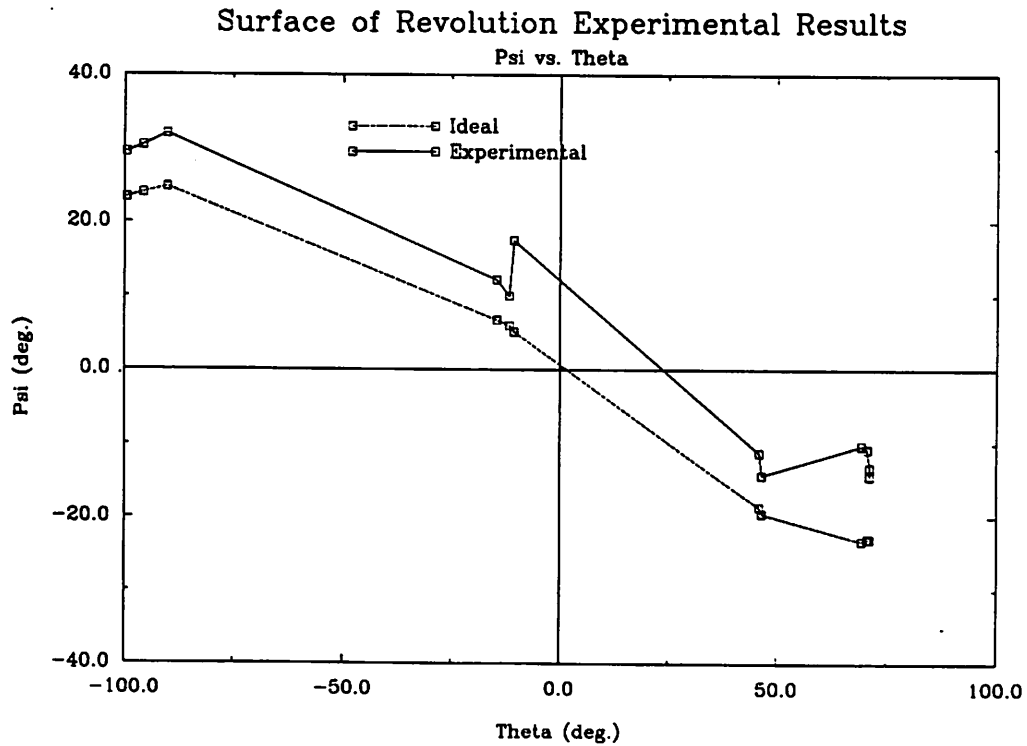


Figure 17. Experimental Angle Error

Note the apparent consistent offset that was mentioned in section 7.2.6. The average error was about 8°. The reason for this behavior was unknown.

The rms error between the model strains and actual strains on our RobotWorld setup was significantly worse than data taken from our setup on a machinist's table. Error on RobotWorld was in the 3-4% of full scale range, while data on the machinist's table was in the 1-3% range. Possibilities for this difference include the fact that the sensor could not be applied to the object with a normal force. The strain response to a non-normal force is significantly different than the response to a normal force. Also, the objects we touched on RobotWorld were made of wood while the objects we used with the machinist's table were plastic (different friction properties). In addition, the surface of revolution used on RobotWorld had larger radii than our other test objects. Thus, the contact ellipse was larger for the surface of revolution, and possibly the direction of the contact forces and the differences in the half space and cylindrical geometry could have had more of an effect (see section 7.2.6). The speed of impact of the tactile sensor on the surface of revolution (using RobotWorld's slowest possible motion) was higher than on the machinist's table. Finally, the RobotWorld motors were a potential noise source. Stray magnetic fields could have corrupted the measurement of the capacitive elements.

8. References

- [1] Peter K. Allen, "Sensing and Describing 3-D Structure," *IEEE International Conference on Robotics and Automation*, San Francisco, CA, April, 1986.
- [2] Peter K. Allen and Kenneth S. Roberts, "Haptic Object Recognition Using a Multi-Fingered Dextrous Hand," *IEEE Conference on Robotics and Automation*, Phoenix, Arizona, 1989.
- [3] Michael Brady, Jean Ponce, and Alan Yuille, "Describing Surfaces," *Proceedings of the 2nd International Symposium on Robotics*, Kyoto, Japan, August, 1984,
- [4] Richard Cole and Chee K. Yap, "Shape from Probing" *Journal of Algorithms*, vol. 8, pp. 19-38, 1987.
- [5] R.E. Ellis. "A Tactile Sensing Strategy for Model-Based Object Recognition," *COINS Technical Report*, pp. 87-96, University of Massachusetts, Amherst, 1987.
- [6] R. E. Ellis, "Uncertainty Estimates for Polyhedral Object Recognition," *IEEE Conference on Robotics and Automation*, Phoenix, Arizona, 1989.
- [7] O.D. Faugeras and M. Hebert, "The Representation, Recognition, and Positioning of 3-D Shapes from Range Data," *International Journal of Robotics Research*, vol. 5, no. 3, Fall, 1986.
- [8] Ronald S. Fearing, A. Rise, and T.O. Binford, "A Tactile Sensing Finger Tip for a Dextrous Hand," *5th SPIE Intelligent Robotics and Computer Vision*, Cambridge, MA, October, 1986.
- [9] R.S. Fearing, "Tactile Sensing for Shape Interpretation," in *Dextrous Robot Hands* edited by S.T. Venkataraman and T. Iberall, New York: Springer-Verlag 1990.
- [10] Ronald S. Fearing and T.O. Binford, "Using a Cylindrical Tactile Sensor for Determining Curvature," *IEEE International Conference on Robotics and Automation*, Philadelphia, PA, April 1988.
- [11] P. C. Gaston and T. Lozano-Perez, "Tactile Recognition and Localization Using Object Models: the Case of Polyhedra on a Plane," *M.I.T. A.I. Memo*, vol. 705, March, 1983.

- [12] E. F. Gobel, *Rubber Springs Design*, London: Newnes-Butterworths 1974.
- [13] W. Eric L. Grimson, "On the Recognition of Parametrized Objects," *International Symposium on Robotics Research*, 1987.
- [14] Martin M. Lipschutz, *Differential Geometry*, New York: McGraw-Hill 1969.
- [15] Ramakant Nevatia, *Machine Perception*, Englewood Cliffs, NJ: Prentice-Hall, 1982.
- [16] Jean Ponce, David Chelberg, and Wallace Mann, "Invariant Properties of Straight Homogeneous Generalized Cylinders and their Contours," *IEEE Transactions on Pattern Analysis and Machine Intelligence*, September, 1989.
- [17] Harry Printz, "Finding the Orientation of a Cone or Cylinder," *Proceedings of the IEEE Computer Society Workshop on Computer Vision*, Miami Beach, Florida, November, 1987.
- [18] Kashipati Rao and Ramakant Nevatia, "Computing Volume Descriptions from Sparse 3-D Data," *International Journal of Computer Vision*, vol. 2, no. 1, pp. 33-50, 1988.